Precise measurements of direct *CP* violation, *CPT* symmetry, and other parameters in the neutral kaon system

E. Abouzaid,[4] M. Arenton,[11] A. R. Barker,[5,*] M. Barrio,[4] L. Bellantoni,[7] E. Blucher,[4] G. J. Bock,[7] C. Bown,[4] E. Cheu,[1] R. Coleman,[7] M. D. Corcoran,[9] B. Cox,[11] A. R. Erwin,[12] C. O. Escobar,[3] A. Glazov,[4,†] A. Golossanov,[11] R. A. Gomes,[3] P. Gouffon,[10] J. Graham,[4] J. Hamm,[12] Y. B. Hsiung,[7] D. A. Jensen,[7] R. Kessler,[4] K. Kotera,[8] J. LaDue,[5] A. Ledovskoy,[11] P. L. McBride,[7] E. Monnier,[4,‡] H. Nguyen,[7] R. Niclasen,[5] D. G. Phillips II,[11] V. Prasad,[4] X. R. Qi,[7] E. J. Ramberg,[7] R. E. Ray,[7] M. Ronquest,[11] A. Roodman,[4] E. Santos,[10] P. Shanahan,[7] P. S. Shawhan,[4] W. Slater,[2] D. Smith,[11] N. Solomey,[4] E. C. Swallow,[4,6] S. A. Taegar,[1] P. A. Toale,[5] R. Tschirhart,[7] Y. W. Wah,[4] J. Wang,[1] H. B. White,[7] J. Whitmore,[7] M. J. Wilking,[5] B. Winstein,[4] R. Winston,[4] E. T. Worcester,[4] T. Yamanaka,[8] E. D. Zimmerman,[5] and R. F. Zukanovich[10]

[1]*University of Arizona, Tucson, Arizona 85721, USA*
[2]*University of California at Los Angeles, Los Angeles, California 90095, USA*
[3]*Universidade Estadual de Campinas, Campinas, Brazil 13083-970*
[4]*The Enrico Fermi Institute, The University of Chicago, Chicago, Illinois 60637, USA*
[5]*University of Colorado, Boulder, Colorado 80309, USA*
[6]*Elmhurst College, Elmhurst, Illinois 60126, USA*
[7]*Fermi National Accelerator Laboratory, Batavia, Illinois 60510, USA*
[8]*Osaka University, Toyonaka, Osaka 560-0043, Japan*
[9]*Rice University, Houston, Texas 77005, USA*
[10]*Universidade de São Paulo, São Paulo, Brazil 05315-970*
[11]*The Department of Physics and Institute of Nuclear and Particle Physics, University of Virginia, Charlottesville, Virginia 22901, USA*
[12]*University of Wisconsin, Madison, Wisconsin 53706, USA*

We present precise tests of *CP* and *CPT* symmetry based on the full data set of $K \to \pi\pi$ decays collected by the KTeV experiment at Fermi National Accelerator Laboratory during 1996, 1997, and 1999. This data set contains 16×10^6 $K \to \pi^0\pi^0$ and 69×10^6 $K \to \pi^+\pi^-$ decays. We measure the direct *CP* violation parameter $\mathrm{Re}(\epsilon'/\epsilon) = (19.2 \pm 2.1) \times 10^{-4}$. We find the $K_L - K_S$ mass difference $\Delta m = (5270 \pm 12) \times 10^6 \hbar$ s^{-1} and the K_S lifetime $\tau_S = (89.62 \pm 0.05) \times 10^{-12}$ s. We also measure several parameters that test *CPT* invariance. We find the difference between the phase of the indirect *CP* violation parameter ϵ and the superweak phase: $\phi_\epsilon - \phi_{\mathrm{SW}} = (0.40 \pm 0.56)°$. We measure the difference of the relative phases between the *CP* violating and *CP* conserving decay amplitudes for $K \to \pi^+\pi^-$ (ϕ_{+-}) and for $K \to \pi^0\pi^0$ (ϕ_{00}): $\Delta\phi = (0.30 \pm 0.35)°$. From these phase measurements, we place a limit on the mass difference between K^0 and $\bar{K}^0$: $\Delta M < 4.8 \times 10^{-19}$ GeV/c^2 at 95% C.L. These results are consistent with those of other experiments, our own earlier measurements, and *CPT* symmetry.

I. INTRODUCTION

Since the 1964 discovery of *CP* violation in $K_L \to \pi^+\pi^-$ decay [1], significant experimental effort has been devoted to understanding the mechanism of *CP* violation. Early experiments showed that the observed effect was due mostly to a small asymmetry between the $K^0 \to \bar{K}^0$ and $\bar{K}^0 \to K^0$ transition rates, which is referred to as indirect *CP* violation. Decades of additional effort were required to demonstrate the existence of direct *CP* violation in a decay amplitude. This paper reports the final measurement of direct *CP* violation by the KTeV experiment (E832) at Fermilab.

Direct *CP* violation can be detected by comparing the level of *CP* violation for different decay modes. The parameters ϵ and ϵ' are related to the ratio of *CP* violating to *CP* conserving decay amplitudes for $K \to \pi^+\pi^-$ and $K \to \pi^0\pi^0$:

$$\eta_{+-} \equiv \frac{A(K_L \to \pi^+\pi^-)}{A(K_S \to \pi^+\pi^-)} \approx \epsilon + \epsilon',$$

$$\eta_{00} \equiv \frac{A(K_L \to \pi^0\pi^0)}{A(K_S \to \pi^0\pi^0)} \approx \epsilon - 2\epsilon', \qquad (1)$$

where ϵ is a measure of indirect *CP* violation, which is common to both decay modes. The relation among the complex parameters η_{+-}, η_{00}, ϵ, and ϵ' is illustrated in Fig. 1.

If *CPT* symmetry holds, the phase of ϵ is equal to the "superweak" phase:
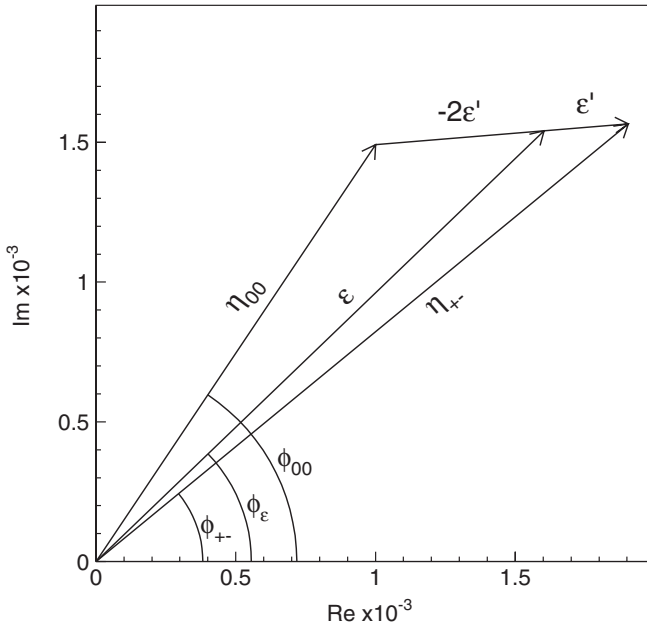
FIG. 1.   Diagram of *CP* violating kaon parameters. For this illustration, the ϵ parameter has the central value measured by KTeV and the value of ϵ' is scaled by a factor of 50. Although they appear distinct in this diagram, note that ϕ_{+-} and ϕ_{00} are consistent with each other within experimental errors.

$$\phi_{SW} \equiv \tan^{-1}(2\Delta m / \Delta\Gamma), \qquad (2)$$

where $\Delta m \equiv m_L - m_S$ is the $K_L - K_S$ mass difference and $\Delta\Gamma = \Gamma_S - \Gamma_L$ is the difference in the decay widths.

The quantity ϵ' is a measure of direct *CP* violation, which contributes differently to the $\pi^+\pi^-$ and $\pi^0\pi^0$ decay modes, and is proportional to the difference between the decay amplitudes for $K^0 \to \pi^+\pi^-(\pi^0\pi^0)$ and $\bar{K}^0 \to \pi^+\pi^-(\pi^0\pi^0)$. Measurements of $\pi\pi$ phase shifts [2] show that, in the absence of *CPT* violation, the phase of ϵ' is approximately equal to that of ϵ. Therefore, $\text{Re}(\epsilon'/\epsilon)$ is a measure of direct *CP* violation and $\text{Im}(\epsilon'/\epsilon)$ is a measure of *CPT* violation.

Experimentally, $\text{Re}(\epsilon'/\epsilon)$ is determined from the double ratio of the two pion decay rates of K_L and K_S:

$$\frac{\Gamma(K_L \to \pi^+\pi^-)/\Gamma(K_S \to \pi^+\pi^-)}{\Gamma(K_L \to \pi^0\pi^0)/\Gamma(K_S \to \pi^0\pi^0)} = \left|\frac{\eta_{+-}}{\eta_{00}}\right|^2$$
$$\approx 1 + 6\,\text{Re}(\epsilon'/\epsilon). \qquad (3)$$

For small $|\epsilon'/\epsilon|$, $\text{Im}(\epsilon'/\epsilon)$ is related to the phases of η_{+-} and η_{00} by

$$\phi_{+-} \approx \phi_\epsilon + \text{Im}(\epsilon'/\epsilon),$$
$$\phi_{00} \approx \phi_\epsilon - 2\,\text{Im}(\epsilon'/\epsilon), \qquad (4)$$
$$\Delta\phi \equiv \phi_{00} - \phi_{+-} \approx -3\,\text{Im}(\epsilon'/\epsilon).$$

The standard model accommodates both direct and indirect *CP* violation [3–5]. Most recent standard model predictions for $\text{Re}(\epsilon'/\epsilon)$ are less than 30×10^{-4} [6–15];

however, there are large hadronic uncertainties in these calculations. Experimental results have established that $\text{Re}(\epsilon'/\epsilon)$ is nonzero [16–20]. The previous result from KTeV, which was based on about half of the KTeV data set, is $\text{Re}(\epsilon'/\epsilon) = (20.7 \pm 2.8) \times 10^{-4}$ [20]. This result was published in 2003 and will be referred to in this text as "KTeV03." The result based on all data from NA48 at CERN is $\text{Re}(\epsilon'/\epsilon) = (14.7 \pm 2.2) \times 10^{-4}$ [19].

This paper reports the final measurement of $\text{Re}(\epsilon'/\epsilon)$ by KTeV. The measurement is based on 85×10^6 reconstructed $K \to \pi\pi$ decays collected in 1996, 1997, and 1999. This full sample is 2 times larger than, and contains, the sample on which the KTeV03 results are based. We also present measurements of the kaon parameters Δm and τ_S and tests of *CPT* symmetry based on measurements of $\Delta\phi$ and $\phi_\epsilon - \phi_{SW}$. Using our phase measurements, we place a limit on the mass difference between K^0 and $\bar{K}^0$.

For this analysis we have made significant improvements to the data analysis and the Monte Carlo simulation. The full data set, including the data used in KTeV03, has been reanalyzed using the improved reconstruction and simulation. These results supersede the previously published KTeV03 results [20], which were based on data from 1996 and 1997.

This paper describes the KTeV experiment in Sec. II, the analysis technique in Sec. III, and the extraction of physics results in Sec. IV. We emphasize changes and improvements since the KTeV03 publication. We will refer to [20] for some details that have not changed since KTeV03. Section V presents the final KTeV results, including correlations between the parameters and cross-checks of the results. Section VI is a summary and discussion of the results. The appendix contains a discussion of the dependence of our measurements on details of kaon regeneration.

II. MEASUREMENT TECHNIQUE AND APPARATUS

A. Overview

The measurement of $\text{Re}(\epsilon'/\epsilon)$ requires a source of K_L and K_S decays and a detector to reconstruct the charged $(\pi^+\pi^-)$ and neutral $(\pi^0\pi^0)$ final states. The strategy of the KTeV experiment is to produce two identical K_L beams and then to pass one of the beams through a "regenerator" that is about two hadronic interaction lengths long. The beam that passes through the regenerator is called the regenerator beam, and the other beam is called the vacuum beam. The regenerator creates a coherent $|K_L\rangle + \rho|K_S\rangle$ state, where ρ, the regeneration amplitude, is a physical property of the regenerator. The regenerator is designed such that most of the $K \to \pi\pi$ decays downstream of the regenerator are from the K_S component. The charged spectrometer is the primary detector for reconstructing $K \to \pi^+\pi^-$ decays and the pure cesium iodide (CsI) calorimeter is used to reconstruct the four photons from $K \to \pi^0\pi^0$ decays. A Monte Carlo simulation is used to

correct for the average acceptance difference between $K \to \pi\pi$ decays in the two beams, which results from the very different K_L and K_S lifetimes. The decay-vertex distributions provide a critical check of the simulation. The measured quantities are the vacuum-to-regenerator "single ratios" for $K \to \pi^+\pi^-$ and $K \to \pi^0\pi^0$ decay rates. These single ratios are proportional to $|\eta_{+-}/\rho|^2$ and $|\eta_{00}/\rho|^2$, respectively, and the ratio of these two quantities gives $\mathrm{Re}(\epsilon'/\epsilon)$ via Eq. (3).

B. KTeV experiment

The KTeV kaon beams are produced by a beam line of magnets, absorbers, and collimators that act on the products of a proton beam incident on a fixed target. The 800 GeV/c proton beam, provided by the Fermilab Tevatron, has a 53 MHz rf structure so that the protons arrive in $\sim$1 ns wide "buckets" at 19 ns intervals. This beam is incident on a beryllium oxide (BeO) target that is about one proton interaction length long. Immediately downstream of the target, the beam consists of protons, muons, and other charged particles, neutral kaons, neutrons, photons, and hyperons. This beam is collimated into two beams and the nonkaon component is reduced by magnets and absorbers in a 100 m long beam line. At the start of the fiducial decay region, 120 m downstream of the target, the average kaon momentum is about 70 GeV/c. The neutron-to-kaon ratio is 1.3 in the vacuum beam and 0.8 in the regenerator beam. The KTeV beams and the beam line elements that produce them are described in detail in [20].

KTeV can reconstruct kaon decays that occur in an evacuated decay region 90–160 m downstream of the target. Figure 2 is a schematic of the detector. In the KTeV coordinate system, the positive x axis points to the left if the observer is facing downstream, the positive y axis points up, and the positive z axis points downstream from the target. Near the upstream end of the decay region,
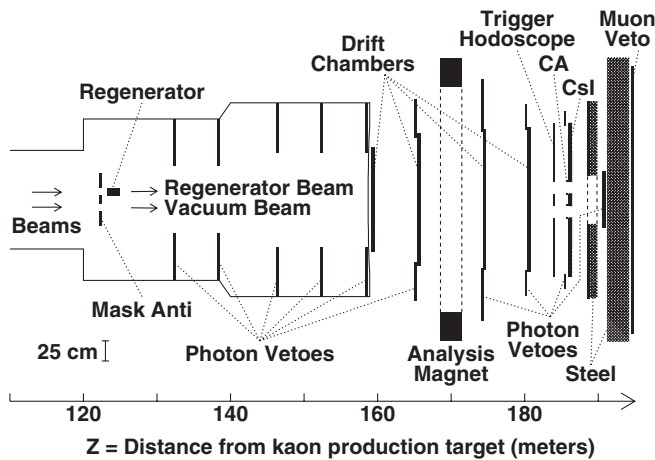
the regenerator alternates between the two beams to minimize acceptance differences between decays in the vacuum and regenerator beams. The charged spectrometer and CsI calorimeter are located downstream of the vacuum window at the end of the decay region. The decay region and primary detectors are surrounded by a system of photon veto detectors to detect particles with trajectories that miss the CsI calorimeter. The major detector elements are described in more detail in the following paragraphs.

The regenerator consists mainly of $8410 \times 10 \times 2$ cm^3 scintillator modules as seen in Fig. 3(a). Its primary purpose is to provide K_S regeneration, but it is also used as part of the trigger and veto systems. Each module is viewed by two photomultiplier tubes (PMTs), one from above and one from below. The downstream end of the regenerator has a lead-scintillator sandwich called the "regenerator Pb module" [Fig. 3(b)], which is also viewed by two PMTs. This last module of the regenerator is used to define a sharp upstream edge for the kaon decay region in the regenerator beam.

The charged spectrometer consists of four drift chambers (DCs) and a dipole magnet. Each drift chamber measures charged-particle positions in both the x and y views. A chamber consists of two planes of horizontal wires to measure y hit coordinates and two planes of vertical wires to measure x hit coordinates; the two x planes and the two y planes are offset to resolve position ambiguities. The DC
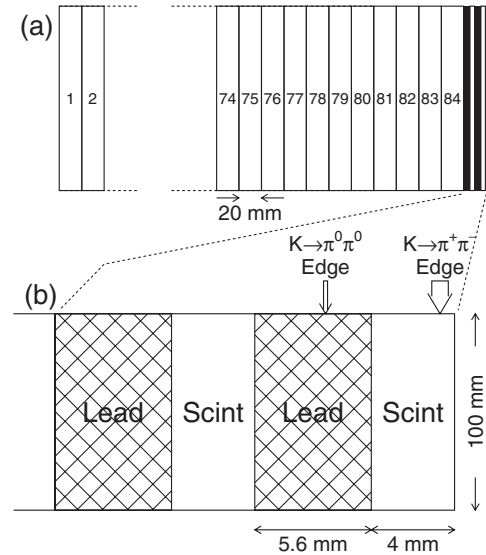
FIG. 3. Diagram of the regenerator. (a) Layout of the 85 regenerator modules, including the lead-scintillator module. (b) Zoomed diagram of the lead-scintillator regenerator module. The PMTs above and below are not shown. The thickness of each lead (scintillator) piece is 5.6 (4.0) mm. The transverse dimension is 100 mm and is not drawn with the same scale as the z axis. The kaon beam enters from the left. The arrows indicate the location and $\pm 1\sigma$ uncertainty of the effective upstream edges for reconstructed $K \to \pi^0\pi^0$ and $K \to \pi^+\pi^-$ decays for 1999 data.

FIG. 2. Schematic of the KTeV detector. Note that the vertical and horizontal scales are different.

FIG. 4. Diagram of drift chamber geometry showing six field wires (open circles) around each sense wire (solid dots). The solid lines illustrate the hexagonal cell geometry; they do not represent any physical detector element.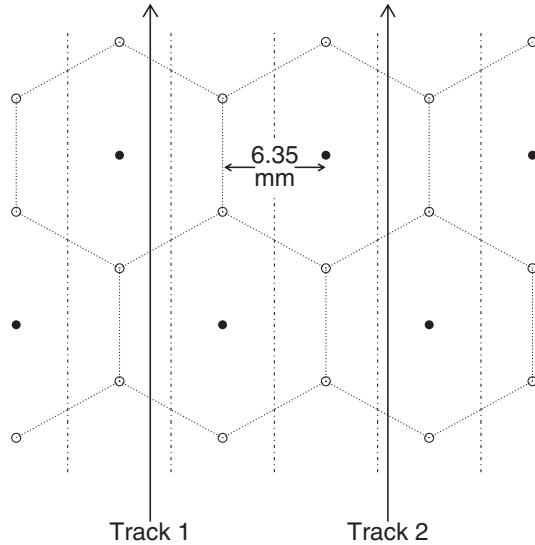 The vertical dashed lines are separated by 6.35 mm and are used to define the track separation cut described in Sec. III B 2.
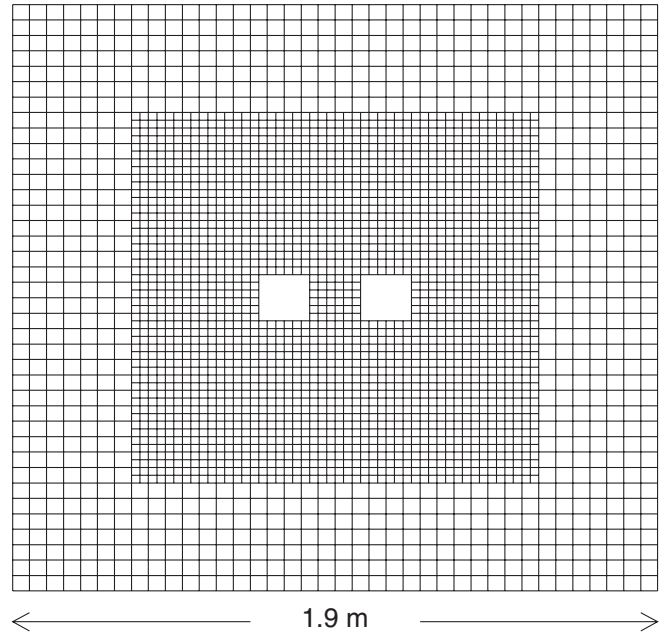

FIG. 5. Beam line view of the KTeV CsI calorimeter, showing the 868 larger outer crystals and the 2232 smaller inner crystals. Each beam hole size is 15×15 cm^2 and the two beam hole centers are separated by 0.3 m. The positive z direction is into the page.

planes have a hexagonal cell geometry formed by six field-shaping wires surrounding one sense wire (Fig. 4). There are a total of 1972 sense wires in the four drift chambers. The cells are 6.35 mm wide, and the drift velocity is about 50 μm/ns. The analyzing magnet imparts a kick of 412 MeV/c in the horizontal plane. The well-known kaon mass is used to set the momentum scale with 10^{-4} precision.

The CsI calorimeter consists of 3100 pure CsI crystals viewed by photomultiplier tubes. The layout of the 1.9×1.9 m^2 calorimeter is shown in Fig. 5. There are 2232 2.5×2.5 cm^2 crystals in the central region and 868 5×5 cm^2 crystals surrounding the smaller crystals. The crystals are all 50 cm (27 radiation lengths) long. Each crystal is wrapped in 12 μm, partially blackened, aluminized Mylar in a manner designed to make the longitudinal response of each crystal as uniform as possible. The calorimeter is read out by custom digitizing electronics placed directly behind the PMTs [21]. Momentum-analyzed electrons and positrons from $K_L \to \pi^\pm e^\mp \nu$ (K_{e3}) decays are used to calibrate the CsI energy scale to 0.02%.

An extensive veto system is used to reject events coming from interactions in the regenerator and to reduce background from kaon decays into non-$\pi\pi$ final states such as $K_L \to \pi^\pm \mu^\mp \nu$ and $K_L \to \pi^0 \pi^0 \pi^0$. The veto system consists of a number of lead-scintillator detectors in and around the primary detectors.

KTeV uses a three-level trigger to select events. Level 1 uses fast signals from the detector and introduces no dead time. Level 2 is based on more sophisticated processing from custom electronics and introduces a dead time of

2–3 μs; when an event passes level 2 the entire detector is read out with an average dead time of 15 μs. Level 3 is a software filter; the processors have enough memory that no further dead time is introduced.

Individual triggers are defined to select $K \to \pi^+ \pi^-$ and $K \to \pi^0 \pi^0$ decays; the trigger efficiencies are studied using decays collected in separate minimum-bias triggers. Additional triggers select decays such as $K_L \to \pi^\pm e^\mp \nu$ and $K_L \to \pi^0 \pi^0 \pi^0$ which are used for calibration and acceptance studies. The "accidental" trigger uses a set of counters near the target to collect events based on primary beam activity; these events are uncorrelated with detector signals that come from the beam particles and are used to model the effects of intensity-dependent accidental activity.

Several changes were made to the KTeV experiment to improve data collection efficiency for the 1999 run.

(1) *Neutral beams.*—The proton extraction cycle of the Tevatron was improved from 20 s extractions (or "spills") every 60 s in 1996 and 1997 to 40 s extractions every 80 s in 1999. The maximum available intensity was $\sim 2 \times 10^{11}$ protons per second. In 1999, KTeV chose to take about half of the data at an average intensity of $\sim 1.6 \times 10^{11}$ protons/s and half at a lower average intensity of $\sim 1 \times 10^{11}$ protons/s as a systematic cross-check.

(2) *CsI calorimeter electronics.*—During 1996 and 1997 data taking, individual channels of the custom readout electronics for the CsI calorimeter failed

occasionally. These failures account for half of the 20% data-taking inefficiency during 1996 and 1997. They also affect the data quality and complicate the calibration of the calorimeter. All of the custom electronics were refabricated and installed in the CsI calorimeter in preparation for the 1999 run. The refabrication of the chips was successful; no CsI calorimeter electronics had to be replaced during the 1999 run.

(3) *Drift chambers*.—The drift chambers required some repair due to radiation damage sustained during data taking in 1996 and 1997. About half of one drift chamber was restrung and a second chamber was cleaned. The drift chamber readout electronics were modified to allow the system to run at higher gain without causing the system to oscillate or trigger on noise.

(4) *Helium bags*.—Helium bags are placed between the drift chambers to minimize the matter seen by the neutral beams after leaving the vacuum decay region and to reduce multiple scattering of charged particles. In 1996 and 1997, one of the small helium bags was leaky and contained mostly air by the end of the 1997 run, so it was necessary in the analysis to correct for the increased multiple scattering resulting from this increased material in the detector. The bags were replaced for 1999. This reduction in material traversed by the beams was offset by a change in the buffer gas used in the drift chambers; the total ionization loss upstream of the CsI calorimeter was less than 5 MeV in each year. This energy loss occurs mostly in the scintillator hodoscope just upstream of the CsI calorimeter.

(5) *Trigger*.—In 1999, the trigger was adjusted to select more $K_L \to \pi^+ \pi^- \pi^0$ decays for the measurement of kaon flux attenuation in the regenerator beam, called "regenerator transmission." The improvement of this measurement reduces several systematic uncertainties associated with the fitting procedure as described in Sec. IV B.

C. Monte Carlo simulation

KTeV uses a Monte Carlo (MC) simulation to calculate the detector acceptance and to model background to the signal modes. The different K_L and K_S lifetimes lead to different z-vertex distributions in the vacuum and regenerator beams. We determine the detector acceptance as a function of kaon decay z vertex and energy, including the effects of geometry, detector response, and resolution. To help verify the accuracy of the MC simulation, we collect and study decay modes with approximately 10 times higher statistics than the $K \to \pi\pi$ signal samples: $K_L \to \pi^\pm e^\mp \nu$, $K_L \to \pi^0 \pi^0 \pi^0$, and $K_L \to \pi^+ \pi^- \pi^0$.

The Monte Carlo simulates $K^0 / \bar{K}^0$ generation at the BeO target following the parameterization in [22],

propagates the coherent $K^0 / \bar{K}^0$ state through the absorbers and collimators along the beam line to the decay point, simulates the decay including decays inside the regenerator, traces the decay products through the detector, and simulates the detector response including the digitization of the detector signals and the trigger selection. The parameters of the detector geometry are based both on data and survey measurements. Many aspects of the tracing and detector response are based on samples of detector responses, called "libraries," that are generated with GEANT [23] simulations; the use of libraries keeps the MC relatively fast. The effects of accidental activity are included in the simulation by overlaying data events from the accidental trigger onto the simulated events. The Monte Carlo event format is identical to data and the events are reconstructed and analyzed in the same manner as data. More details of the simulation are available in [20].

Many improvements have been made to the MC simulation since KTeV03 [20]. We have improved the simulation to include finer details of electromagnetic showering in the CsI calorimeter and charged-particle propagation through the detector. These changes are described in detail below.

(1) *Shower library*.—For this analysis, the GEANT-based library used to simulate photon and electron showers in the CsI calorimeter has been improved to simulate the effects of the incident particle angle. The library used for KTeV03 was binned in energy and incident position. There were 325 position bins and six logarithmic energy bins (2, 4, 8, 16, 32, and 64 GeV). The effect of angles was approximated by shifting the incident position based on the angle of incidence. The shower library has now been expanded to include nine angles in x and y (-35 to 35 mrad) for photons and 15 angles in x and y (-85 to 85 mrad) for electrons. Electron angles may be larger than photon angles because of the momentum kick imparted by the analyzing magnet. The position and energy binning is unchanged from KTeV03. Differences between the library angle and the desired angle are accounted for by shifting the incident position. The particle energy cutoff applied in the GEANT shower library generation has been lowered from 600 to 50 keV for electrons; the photon cutoff of 50 keV is unchanged. Sixteen showers per bin have been generated. Energy deposits are corrected for energy lost in the 12 μm Mylar wrapping around the CsI crystals.

The current Monte Carlo produces a significantly better simulation of electromagnetic showers in the CsI calorimeter. Figure 6 shows the data-MC comparison of the fraction of energy in each of the 49 CsI crystals in electron showers relative to the total reconstructed shower energies for electrons from $K_L \to \pi^\pm e^\mp \nu$ decays. The majority of the energy
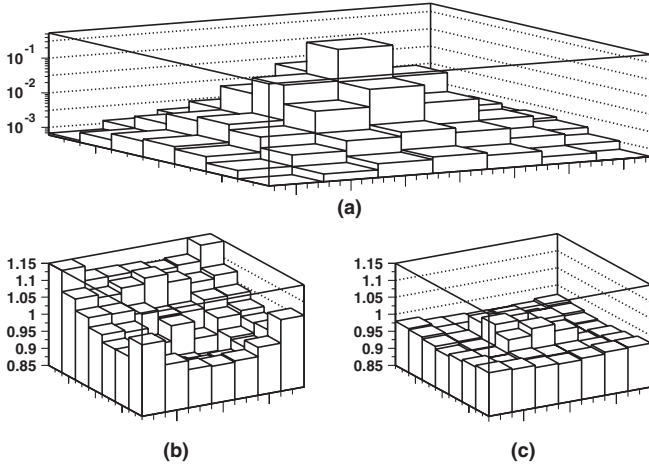
(a)

(b)　　　　　　　　　**(c)**

FIG. 6.　Data-MC comparison of the fraction of energy in each of the 49 CsI crystals in an electron shower. (a) The fraction of energy in each of the 49 CsI crystals in electron showers for the data. (b) KTeV03 data/MC ratio. (c) Current data/MC ratio.
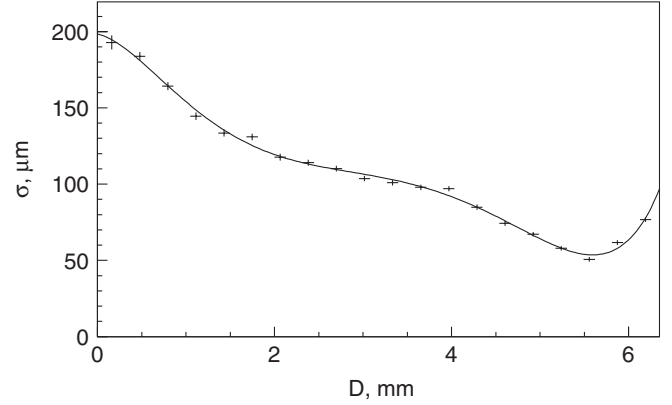

FIG. 7.　Dependence of drift chamber position resolution on position within the cell. D is the distance from the sense wire. Crosses represent the measured central values and uncertainties of the resolution in bins of D, and the line represents a polynomial fit to the data. This fit is used in the simulation to parameterize the position dependence of the position resolution.

is deposited in the central crystal since the Moliere radius of CsI is 3.8 cm. These plots are made for 16–32 GeV electrons with incident angles of 20–30 mrad; the quality of agreement is similar for other energies and angles. The data-MC agreement improves dramatically as seen in Fig. 6. This improvement in the modeling of electromagnetic shower shapes leads to important reductions in the systematic uncertainties associated with the reconstruction of photon showers from $K \rightarrow \pi^0 \pi^0$ decays (see Sec. III C).

(2) *Ionization energy loss*.—In KTeV03, we did not include the effect of ionization energy losses for charged particles in the simulation. In the current simulation, we include the ionization loss for each volume of material in the detector. The total loss up to the surface of the CsI is less than 5 MeV. This is a very small effect for $K \rightarrow \pi^+ \pi^-$ decays but it is important for low-energy electrons used in the calibration of the CsI calorimeter and affects converted photons from $K \rightarrow \pi^0 \pi^0$ decays.

(3) *Bremsstrahlung*.—In KTeV03, the MC included electron bremsstrahlung in materials upstream of the analyzing magnet only. In the current analysis, the bremsstrahlung rate and photon angle in each volume of material in the detector are included in the simulation.

(4) *Delta rays*.—In the KTeV03 simulation, delta rays produced in a drift chamber cell deposited all of their energy in that cell. The MC now has a more complete treatment in which delta rays may scatter into adjacent cells of the drift chamber. High momentum delta rays are traced through the detector like any other particle and low momentum delta rays are simulated using a library created with

GEANT4 [24]. This treatment of delta rays improves our simulation of the distribution of extra in-time hits in the drift chambers.

(5) *Pion interactions*.—The probability for pions to interact hadronically with material in the spectrometer is 0.7%; hadronic interactions in the spectrometer were not simulated in KTeV03. These events are now simulated using a GEANT-based library which contains a list of secondary particles produced by each hadronic interaction. An average of nine secondary particles are produced per interaction; these secondary particles are read in from the shower library and traced through the rest of the detector like any other particle. Events with pion interactions typically trigger the photon veto system and so do not pass selection criteria in the analysis.

(6) *Fringe fields*.—The simulation of fringe fields from the analysis magnet has been refined. Fringe fields from the analysis magnet inside the vacuum tank and between all four drift chambers have been measured and are now simulated. The maximum strength of the fringe field in these regions is comparable to the Earth's magnetic field. The fringe field simulation improves the MC description of the azimuthal dependence of the $\pi^+ \pi^-$ invariant mass for $K \rightarrow \pi^+ \pi^-$ data.

(7) *Position resolution*.—The position resolution of the drift chambers is dependent upon position within the cell as shown in Fig. 7. In KTeV03, the resolution was treated as flat across the cell; the position dependence of the resolution is now simulated. The position dependence of the resolution is also considered in the analysis of $K \rightarrow \pi^+ \pi^-$ data; this is described in Sec. III B.

The position resolution of CsI calorimeter clusters in the MC is slightly worse than in the data. To better match the resolutions, we artificially improve the resolution of the MC by 9%. This is done by moving the reconstructed position toward the generated particle position.

III. DATA ANALYSIS

The analysis is designed to identify $K \to \pi\pi$ decays while removing poorly reconstructed events that are difficult to simulate and to reject background. For each decay mode, the same requirements are applied to decays in the vacuum and regenerator beams, so that most systematic uncertainties cancel in the single ratios used to measure $|\eta_{+-}/\rho|^2$ and $|\eta_{00}/\rho|^2$. The following sections describe the analysis and the associated systematic uncertainties in $\mathrm{Re}(\epsilon'/\epsilon)$.

A. Common features

Although many details of the charged and neutral decay mode analyses are different, several features are common to reduce systematic uncertainties. We select an identical 40–160 GeV/c kaon momentum range for both the charged and neutral decay modes. We also use the same z-vertex range of 110–158 m from the target for each decay mode. To simplify the treatment of background from kaons that scatter in the regenerator, the veto requirements for the charged and neutral mode analyses are made as similar as possible.

When discussing systematic uncertainties, we follow the same procedure as in KTeV03 [20]. We estimate a potential shift $s \pm \sigma_s$, where s is the shift in $\mathrm{Re}(\epsilon'/\epsilon)$ and σ_s is the statistical uncertainty on s. We assign a symmetric systematic error Δ_s such that the range $[-\Delta_s, +\Delta_s]$ includes 68.3% of the area of a Gaussian with mean s and width σ_s.

B. Charged reconstruction and systematics

The $K \to \pi^+\pi^-$ analysis consists primarily of the reconstruction of tracks in the spectrometer; the vertices and momenta of the tracks are used to calculate kinematic quantities describing the decay. The CsI calorimeter is used for particle identification by comparing the reconstructed cluster energy to the measured track momentum. The analysis requirements provide clean identification of well-reconstructed $K \to \pi^+\pi^-$ events with little background contamination. The cuts are sufficiently loose to reduce systematics from modeling of resolution tails. The $K \to \pi^+\pi^-$ reconstruction and event selection are described in the following sections; more details of the analysis are found in [20].

1. $K \to \pi^+\pi^-$ reconstruction

The spectrometer reconstruction begins by finding tracks separately in the x and y views. Tracks with missing

hits or other defects can be reconstructed; ~40% of events have at least one tracking flaw, yet the overall single-track reconstruction inefficiency is about ~1%. Track segments are found in the two drift chambers upstream of the magnet and the two drift chambers downstream of the magnet; these segments are then extrapolated to the center of the magnet. We require the extrapolated segments to match within 6 mm at the magnet midplane to form a combined track; they typically match to within 0.5 mm. Each particle momentum is determined from the track bend angle in the magnet and a map of the magnetic field.

The process of finding track segments depends on the alignment and calibration of the drift chambers. For the current analysis, we made new measurements of the drift chamber sizes and rotations. The survey of the wire positions used a large coordinate measurement machine with a camera and magnifying lens mounted on the end of a movable arm. The measured drift chamber size is about 0.02% larger than the nominal value found by scaling the 6.35 mm "cell" size. The relative nonorthogonality between DC1 and DC2 is limited to ± 30 μrad. The uncertainty in $\mathrm{Re}(\epsilon'/\epsilon)$ associated with the drift chamber alignment and calibration is 0.20×10^{-4}. The momentum measurement uses the known kaon mass as a constraint; the 0.022 MeV/c^2 uncertainty in the kaon mass corresponds to an uncertainty in $\mathrm{Re}(\epsilon'/\epsilon)$ of 0.10×10^{-4}.

If two x tracks and two y tracks are found, the reconstruction continues by extrapolating both sets of tracks upstream to define vertices projected on the $x - z$ and $y - z$ planes. The difference between these two projections, Δz_{vtx}, is used to define a vertex χ^2:

$$\chi^2_{\mathrm{vtx}} \equiv (\Delta z_{\mathrm{vtx}}/\sigma_{\Delta z})^2, \tag{5}$$

where $\sigma_{\Delta z}$ is the resolution of Δz_{vtx}. This resolution depends on momentum and opening angle and accounts for multiple scattering effects. The two x tracks and two y tracks are assumed to originate from a common vertex if $\chi^2_{\mathrm{vtx}} < 100$.

To determine the full particle trajectory, the x and y tracks are matched to each other based on their projections to the CsI; the projected track positions must match CsI cluster positions to within 7 cm.

An event is assigned to the regenerator beam if the regenerator x position has the same sign as the x coordinate of the kaon trajectory at the downstream face of the regenerator; otherwise, the event is assigned to the vacuum beam.

In KTeV03 [20], the track segments were reconstructed assuming that the position resolution of the drift chambers does not depend on the hit position within a chamber cell. To check this assumption, a special data sample was collected with the magnetic field turned off. Three chambers are used to reconstruct straight tracks and these tracks are compared to the hits reconstructed in the fourth chamber. The resulting position resolution (see Fig. 7) shows a

significant dependence on the distance between the track and the sense wire. Tracks passing close to a sense wire have worse resolution because of the time separation of drift electrons reaching the sense wire. The variation of the resolution for tracks close to the boundary of a drift cell can be partly explained by the electric field configuration. The drift-time-dependent resolution is included in the MC and is used for the track segment reconstruction in the current analysis. The new resolution measurement improves reconstruction of the z vertex and track momentum. For example, the width of the $\pi^+\pi^-$ invariant mass is reduced by $\sim 14\%$; this improvement is more significant for higher momentum kaons where it reaches $\sim 25\%$.

The kaon decay vertex position and the momenta of the two tracks forming the vertex are used to calculate the $\pi^+\pi^-$ invariant mass, their energy, and p_T^2, the sum of their momenta transverse to the beam direction.

2. $K \to \pi^+\pi^-$ selection

The $K \to \pi^+\pi^-$ event selection begins with the three-level trigger during data taking. Level 1 uses hits in the trigger hodoscopes and the drift chambers to select events consistent with two charged particles coming from the decay of a kaon that did not undergo large angle scattering in the defining collimator or regenerator prior to the decay. Level 2 uses custom hit counting electronics and a track finding system to select events with two tracks from a common vertex. The vertex requirement at trigger level is loose compared to the selection criteria in the offline analysis. The inefficiencies of the level 1 and level 2 triggers are studied using $K_L \to \pi^\pm e^\mp \nu$ decays from minimum-bias triggers. The uncertainty in $\mathrm{Re}(\epsilon'/\epsilon)$ associated with level 1 and level 2 event selection is 0.2×10^{-4}. The level 3 software filter reconstructs two charged tracks and makes loose
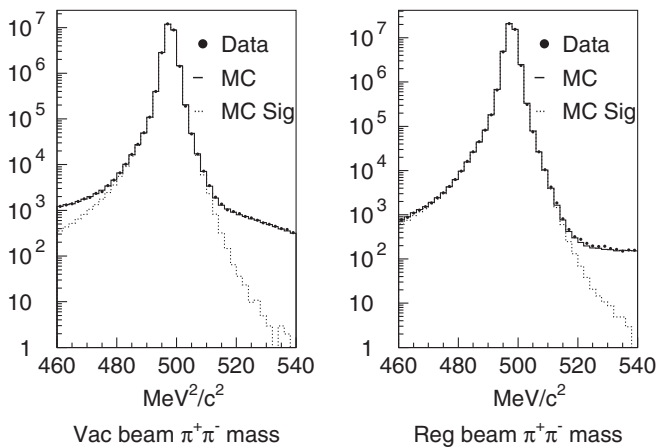
cuts on reconstructed mass and particle identification. To measure the level 3 inefficiency of the $K \to \pi^+\pi^-$ trigger, we perform the full offline analysis on "random accepts," a prescaled subset of the $K \to \pi^+\pi^-$ trigger that has no level 3 requirement. We find that the bias in $\mathrm{Re}(\epsilon'/\epsilon)$ from the level 3 trigger inefficiency is $(0.30 \pm 0.12) \times 10^{-4}$. We correct $\mathrm{Re}(\epsilon'/\epsilon)$ for this bias and assign an uncertainty in $\mathrm{Re}(\epsilon'/\epsilon)$ of 0.12×10^{-4}.

The offline selection criteria for $K \to \pi^+\pi^-$ decays are tighter than those imposed by the trigger. The $K \to \pi^+\pi^-$ analysis requirements and any associated systematic uncertainties in $\mathrm{Re}(\epsilon'/\epsilon)$ are described in the following paragraphs.

We make a number of cuts on energy deposits in the veto detectors. The most important veto requirements are the muon veto cuts, which suppress background from $K_L \to \pi^\pm \mu^\mp \nu_\mu$ decays, and the regenerator cuts, which reduce background from scattered kaons. Additional veto cuts are made for consistency with the $K \to \pi^0\pi^0$ analysis.

We also use the spectrometer and the calorimeter as "veto detectors." We reject events with any tracks other than those from the vertex. We require the ratio of reconstructed cluster energy to track momentum, E/p, to be less than 0.85 to identify the tracks as pions. We require that the track momentum be greater than 8 GeV/c to ensure 100% efficiency for the muon veto detectors. These cuts suppress background from K_{e3} and $K_{\mu3}$ decay modes.

We remove events with $1.112~\mathrm{GeV}/c^2 < m_{p\pi} < 1.119~\mathrm{GeV}/c^2$, where $m_{p\pi}$ is the reconstructed invariant mass assuming the higher momentum particle is a proton. This removes background from $\Lambda \to p\pi^-$ and $\bar{\Lambda} \to \bar{p}\pi^+$ decays where the proton is misidentified as a pion.

Figure 8 shows the $\pi^+\pi^-$ invariant mass distributions for the two beams; we require $488~\mathrm{MeV}/c^2 < m\pi^+\pi^- < 508~\mathrm{MeV}/c^2$. Figure 9 shows the p_T^2 distributions; we

FIG. 8. $\pi^+\pi^-$ invariant mass distribution for $K \to \pi^+\pi^-$ candidate events in the vacuum (left) and regenerator (right) beams. The data distribution is shown as dots, the $K \to \pi^+\pi^-(\gamma)$ signal MC (MC Sig) is shown as a dotted histogram, and the sum of signal and background MC is shown as a solid histogram.
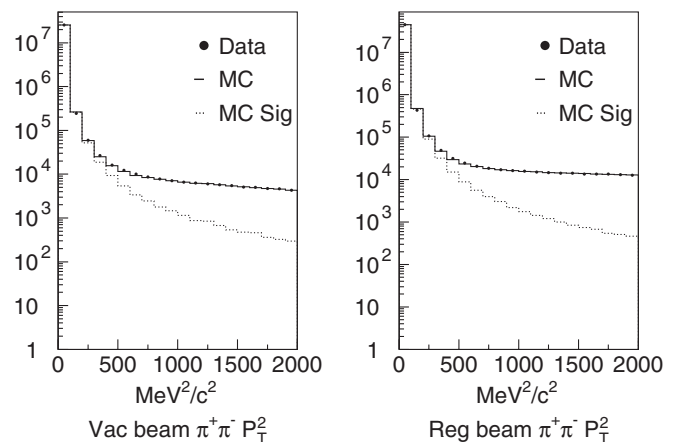

FIG. 9. p_T^2 distribution for $K \to \pi^+\pi^-$ candidate events in the vacuum (left) and regenerator (right) beams. The data distribution is shown as dots, the $K \to \pi^+\pi^-(\gamma)$ signal MC (MC Sig) is shown as a dotted histogram, and the sum of signal and background MC is shown as a solid histogram.

require $p_T^2 < 250$ MeV$^2/c^2$. The p_T^2 requirement is the only $K \to \pi^+ \pi^-$ selection criterion that results in a systematic uncertainty in Re(ϵ'/ϵ). We vary the p_T^2 cut from 125 to 1000 MeV$^2/c^2$ and assign a systematic uncertainty in Re(ϵ'/ϵ) of 0.10×10^{-4} based on the change in Re(ϵ'/ϵ).

To reduce our sensitivity to details of the Monte Carlo simulation, we require track trajectories to be clear of a number of physical apertures. We require that tracks point at least 2 mm into the CsI calorimeter away from the edges of the collar anti detector that surrounds the beam holes and at least 2.9 cm inside the outer edge of the CsI calorimeter. If the vertex position is upstream of the mask anti (MA; see Fig. 2), we require that the track position at the MA be less than 4 cm in x and y from the nominal beam center. We cut away from wires at the edges of the drift chambers. To reduce the possibility of x and y track candidate mismatches, we require that the projections of the tracks at the CsI calorimeter be separated by 6 cm in x and 3 cm in y. We require that decays originate from within one of the beams by requiring that the projection of the vertex (x, y) position along the kaon direction reconstructs inside a 75 cm^2 square at the z of the downstream edge of the regenerator.

We require a minimum separation between the tracks in the x and y views at each drift chamber. This cut is defined in terms of the DC cell through which the track passes; we require that the tracks be separated by at least 3 cells at each chamber. This track separation cut forms a limiting inner aperture and depends on the position of each wire within the drift chambers. The wire spacing is known with an uncertainty of 20 μm. There are variations in the actual wire spacing, which are measured in the data but are not simulated in the Monte Carlo. To determine the effect of these variations, we convolve the track illumination with the wire-cell size to determine the number of events that migrate across the track separation cut in the data but not in the MC. We find that the bias in Re(ϵ'/ϵ) is $(-0.16 \pm 0.12) \times 10^{-4}$; the corresponding uncertainty in Re(ϵ'/ϵ) is $\pm 0.22 \times 10^{-4}$.

The effective regenerator edge, shown in Fig. 3, defines the upstream edge of acceptance for $K \to \pi^+ \pi^-$ decays in the regenerator beam. We find the effective regenerator edge by calculating the probability for two minimum ionizing pions to escape the last piece of scintillator without depositing enough energy to be vetoed. This calculation depends on the measured average energy deposit of a muon passing through the regenerator Pb module, the fraction of energy coming from the last piece of scintillator due to the geometry of the phototube placement on the Pb module, the value of the trigger threshold, and the value of the offline cut on the energy deposit in the Pb module. We find the effective regenerator edge to be (1.65 ± 0.4) mm upstream of the physical edge in 1997 and (0.7 ± 0.4) mm upstream of the physical edge in 1999. The difference in effective edges is due to different offline cuts on the energy

TABLE I. Summary of systematic uncertainties in Re(ϵ'/ϵ) from the $K \to \pi^+ \pi^-$ analysis. The final systematic uncertainties for the combined data set are listed in the column labeled "Full." For those uncertainties that are also evaluated separately in the two years, the individual uncertainties are shown to facilitate comparison with the KTeV03 result.

Source	Error on Re(ϵ'/ϵ) ($\times 10^{-4}$)			
			Current result	
	KTeV03 result	1997	1999	Full
L1 and L2 trigger	0.20	0.20	0.20	0.20
L3 trigger	0.54	0.20	0.14	0.12
Alignment and calibration	0.28	0.20		0.20
Momentum scale	0.16	0.10		0.10
p_T^2	0.25	0.10		0.10
DC efficiency modeling	0.37	0.15		0.15
DC resolution modeling	0.15	0.15		0.15
Background	0.20	0.20		0.20
Wire spacing	0.22	0.22		0.22
Reg edge	0.20	0.20	0.20	0.20
Acceptance	0.79	0.87	0.25	0.41
Upstream z	$\cdots$	0.33	0.48	0.40
Monte Carlo statistics	0.41	0.28	0.28	0.20
Total	1.26	1.12	0.82	0.81

deposit in the Pb module, which are required because of slight detector differences between the two years. In 1997, the edge is defined by the trigger threshold. In 1999, a tight offline cut is applied. We evaluate the uncertainty in this measurement by varying the trigger threshold and the fraction of energy coming from the last piece of scintillator by $\sim$15% each. The 0.4 mm uncertainty in the position of the effective regenerator edge leads to an uncertainty in Re(ϵ'/ϵ) of 0.20×10^{-4}.

We estimate the systematic uncertainty in Re(ϵ'/ϵ) associated with the Monte Carlo simulation of drift chamber efficiencies by generating separate sets of MC in which scattering, DC efficiency maps, and accidental activity are turned off. We take 10% of the resulting variation in Re(ϵ'/ϵ), 0.15×10^{-4}, to be the systematic uncertainty associated with the simulation of drift chamber efficiencies. We vary the simulated drift chamber resolutions by 5% and, from the resulting variation in Re(ϵ'/ϵ), we assign a systematic error of 0.15×10^{-4}.

The systematic uncertainties in Re(ϵ'/ϵ) associated with the $K \to \pi^+ \pi^-$ analysis are summarized in Table I. The total systematic uncertainty associated with the $K \to \pi^+ \pi^-$ analysis is 0.81×10^{-4}; this is reduced by $\sim$35% from KTeV03.

C. Neutral reconstruction and systematics

To reconstruct $K \to \pi^0 \pi^0$ decays, we first identify four clusters of energy in the calorimeter and reconstruct the

energies and positions of the photons associated with each cluster. A number of corrections are then made to the measured cluster energies based on our knowledge of the CsI calorimeter performance and the reconstruction algorithm. We use the cluster positions and energies along with the well-known pion mass to determine which pair of photons is associated with which neutral pion from the kaon decay and to calculate the decay vertex, the center of energy, and the $\pi^0\pi^0$ invariant mass. The precision of the CsI calorimeter energy and position reconstruction is crucial to the $K \to \pi^0\pi^0$ analysis and has been improved significantly since KTeV03. Section III C 1 gives details of the CsI calorimeter reconstruction, Sec. III C 2 describes the reconstruction of $K \to \pi^0\pi^0$ decays, Sec. III C 3 describes the selection criteria for $K \to \pi^0\pi^0$ decays, and Sec. III C 4 describes the systematic uncertainties associated with the CsI calorimeter energy reconstruction.

1. CsI calorimeter energy and position reconstruction

The first step in reconstructing clusters is to determine the energy deposited in each crystal of the CsI calorimeter. We convert the digitized information to an energy using constants for each channel that are determined from the electron calibration. An *in situ* laser, which delivers light at known intensities via quartz fibers to each CsI crystal, is used to calibrate the custom digitizing electronics and to measure the less than 1% spill-to-spill drifts in each channel's gain. The "laser correction" removes these spill-to-spill changes and is applied before any clustering is performed.

We define a "cluster" as a 7×7 array of small crystals or a 3×3 array of large crystals. Clusters near the boundary between the small and large crystals (see Fig. 5) may contain both sizes of crystals; in this case the cluster is defined as a 3×3 array of "large" crystals where the energy deposit in four small crystals is summed to form a large crystal as needed. Each cluster is centered on a "seed crystal," containing the maximum energy deposit among the crystals in the cluster. An initial approximation of the cluster energy is found by summing the energies of the crystals in the cluster.

The x, y position of a cluster is reconstructed by calculating the fraction of energy in neighboring columns and rows of crystals in the cluster. The x, y position algorithm uses a map that is based on assuming a uniform photon illumination across each crystal to convert these ratios to a position within the seed crystal. The position maps are made using isolated clusters from $K \to \pi^0\pi^0$ data; no corrections to the position are applied based on the incident particle angle. The final position is evaluated after all energy corrections are applied.

The raw cluster energy must be corrected for a number of geometric and detector effects. We apply "crystal-level" corrections that adjust the energy in each crystal that makes up the cluster and "cluster-level" corrections,

which are multiplicative corrections to the total cluster energy. Many of the crystal-level corrections rely on "transverse energy maps"; as a function of position within the seed crystal, these maps predict the distribution of energy among the crystals within a cluster . They are made using isolated photon clusters from $K \to \pi^0\pi^0$ data. The crystal-level and cluster-level energy corrections are enumerated below.

(1) *Partial clusters.*—We correct for energy that is missing from the cluster because of crystal energies that are below the readout threshold or because portions of the 3×3 or 7×7 cluster are located in the beam holes or outside the calorimeter. The energy in missing crystals is estimated using the transverse energy maps. The energy in crystals that were below threshold is estimated by a parameterization, which was determined from the data, of the ratio of energy in a crystal to the readout threshold. The fraction of the readout threshold energy predicted to be present in a crystal decreases with distance from the seed crystal and increases logarithmically with cluster energy.

(2) *Out of cone.*—The ~5% "out-of-cone correction" is applied because an electromagnetic shower is not fully contained by the 7×7 small-crystal or 3×3 large-crystal clusters. We determine the out-of-cone correction using the same GEANT simulation used to generate the Monte Carlo shower library (see Sec. II C). The correction is parameterized by a quadratic function of the reconstructed distance of the cluster position from the center of the seed crystal and a linear function of the reconstructed energy. The size of the correction varies by about 1% across the face of a crystal and by about 0.2% per 100 GeV. There is no explicit dependence of the out-of-cone correction on the incident angle; because the reconstructed positions are not corrected for the incident particle angle, the angle effect is included implicitly in our parameterization as a function of the reconstructed position. The correction is generated separately for photons and electrons and for small and large crystals. In KTeV03, the out-of-cone correction was determined for small and large crystals using 8 GeV GEANT showers, but there was no adjustment for the energy, position, or type of the incident particle.

(3) *Longitudinal response.*—We correct the energy in each crystal for the ~5% nonuniformity of response along the length of each CsI crystal. The longitudinal response of each CsI crystal is measured in ten 5-cm z bins using cosmic ray muons that pass vertically through the CsI calorimeter. These muons are detected by a cosmic ray hodoscope consisting of three sets of 3 m-long, overlapping plastic scintillation counters placed above and below the CsI

calorimeter. Typically the crystal response increases with z as the shower nears the PMT. The measured CsI response is convolved with a GEANT prediction of the shower's longitudinal distribution to correct the energy in each crystal. The GEANT shower profiles are generated separately for photons and electrons. There are individual profiles for each crystal position within the cluster; they are binned in the local position relative to the center of the seed crystal and in the same six logarithmic cluster energy bins used in the Monte Carlo (see Sec. II C). The mean shower depth for photons and electrons varies logarithmically with energy. These crystal-by-crystal shower profiles are a significant improvement to the longitudinal uniformity correction; in the KTeV03 analysis, the uniformity correction was applied at cluster level based only on a predicted average longitudinal energy distribution for a whole shower.

(4) *Shared energy.*—For clusters that overlap, we must partition the energy in the shared crystals. The "overlap correction" separates the energy deposited in two or more clusters that share crystals by using the transverse energy maps to predict how much energy each particle contributed to the shared crystals.

The "neighbor correction" estimates the amount of underlying energy in each crystal that comes from nearby clusters that are less than 50 cm away but outside the 3×3 or 7×7 cluster boundary. The correction uses a 13×13 map to predict the energy contribution from neighboring clusters. This map is similar to the transverse energy maps but does not depend on the position within the CsI crystal and is generated using GEANT rather than the data.

We correct clusters near the beam holes for extra energy that comes from nearby clusters that do not share crystals but which leak energy across the beam holes. This correction uses maps made using electrons from $K_L \to \pi^\pm e^\mp \nu$ data.

(5) *Detector effects.*—We correct for a number of detector effects including the observed transverse nonuniformity of energies across each crystal that remains after the out-of-cone correction, the nonlinearity of each channel with energy which remains after the longitudinal uniformity correction, and global time variations in the CsI calorimeter response. These corrections are measured using E/p of electrons from $K_L \to \pi^\pm e^\mp \nu$ decays and are applied multiplicatively to the total cluster energy. The "transverse nonuniformity correction" is made by dividing each cluster seed crystal into a 5×5 grid and measuring the cluster energies of electrons in each of these position bins. A multiplicative correction is applied to the total cluster energy based on the cluster's reconstructed position within the
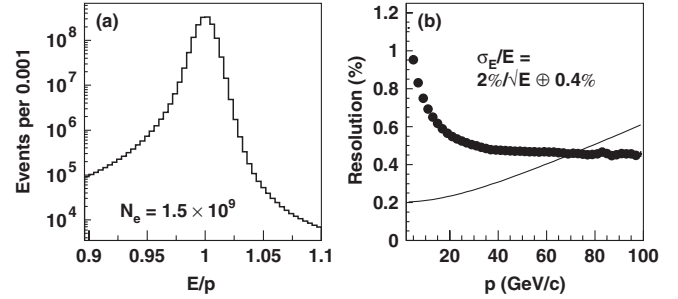

FIG. 10. K_{e3} electrons after all corrections. (a) E/p for 1.5×10^9 electrons. (b) Energy resolution. The fine curve shows the momentum resolution function that has been subtracted from the E/p resolution to find the energy resolution.

seed crystal. The correction is normalized such that the average correction over each crystal (25 bins) is 1.0. The "channel-by-channel linearity correction" removes the residual energy nonlinearity. It is measured separately for each CsI calorimeter channel in data and Monte Carlo. The "spill-by-spill correction" is applied to correct for time variations in the response of the calorimeter as a whole; it is measured and applied separately for each spill. Each of these corrections has a maximum magnitude of less than 1%.

(6) *Photon-electron differences.*—For the $K \to \pi^0 \pi^0$ analysis we apply a "photon correction" that is designed to remove any residual differences between photons and the electrons that are used to calibrate the calorimeter. The correction is based on photons from $K \to \pi^0 \pi^0$ and $K_L \to \pi^0 \pi^0 \pi^0$ decays. It is measured separately for 1996, 1997, and 1999 in nine regions of the calorimeter by fitting each event for the photon energies applying six (four) kinematic constraints for $\pi^0 \pi^0 \pi^0$ ($\pi^0 \pi^0$). The details of the kinematic fit are described in [25]. This correction is most important for photons with energies below 20 GeV; its magnitude is less than 0.2%. The photon correction is new for the current analysis; no correction of photon-electron differences was applied in KTeV03.

The quality of the calibration and the CsI calorimeter performance is evaluated by analyzing electrons from the $K_L \to \pi^\pm e^\mp \nu$ calibration sample with all corrections applied. The electron calibration for 1996, 1997, and 1999 is based on 1.5×10^9 total electrons. Figure 10 shows the E/p distribution and the energy resolution as a function of momentum of these electrons after all corrections. The final energy resolution of the calorimeter is $\sigma_E/E \simeq 2\%/\sqrt{E} \oplus 0.4\%$, where E is in GeV.

2. $K \to \pi^0 \pi^0$ reconstruction

$K \to \pi^0 \pi^0$ and $K_L \to \pi^0 \pi^0 \pi^0$ events are fully reconstructed using the positions and energies of the four or six

photon clusters in the CsI calorimeter. The $K_L \rightarrow \pi^0 \pi^0 \pi^0$ reconstruction is almost identical to the $K \rightarrow \pi^0 \pi^0$ reconstruction, but for simplicity this discussion will be in terms of the $\pi^0 \pi^0$ reconstruction. Using cluster energies and positions, we are able to reconstruct the z vertex of the kaon decay, the (x, y) components of the center of energy of the kaon, the kaon energy, and the $\pi^0 \pi^0$ invariant mass.

We must first determine which pairs of photons are associated in the $K \rightarrow \pi^0 \pi^0$ decay. For four photons, there are three possible pairings. For each pairing we calculate d_{12}, the distance in z between the π^0 decay vertex and Z_{CsI}, the mean shower depth in the CsI crystals. Using the pion mass as a constraint, in the small angle approximation, we find the distance for each pair of photons to be

$$ d_{12} \approx \frac{\sqrt{E_1 E_2}}{m_{\pi^0}} r_{12}, \tag{6} $$

where r_{12} is the transverse distance between the two photons at the CsI calorimeter.

For each pairing, we compare the calculated distance for each candidate pion. In most cases, only the correct pairing will give a consistent distance for both pions. The consistency of the measured distance is quantified using the pairing chi-squared variable:

$$ \chi^2_{\pi^0} \equiv \left(\frac{d_{12} - d_{\text{avg}}}{\sigma_{12}} \right)^2 + \left(\frac{d_{34} - d_{\text{avg}}}{\sigma_{34}} \right)^2. \tag{7} $$

In Eq. (7), d_{ij} is the calculated distance for each pion, d_{avg} is the weighted average of the distance d_{ij} for both pions, and σ_{ij} is the energy-dependent vertex resolution for each pion. We choose the pairing that gives the minimum value of $\chi^2_{\pi^0}$. Using Monte Carlo events, we find that this procedure selects the wrong pairing for less than 0.01% of $K \rightarrow \pi^0 \pi^0$ decays in the final event sample. The z vertex of the kaon decay is taken to be $Z_{\text{CsI}} - d_{\text{avg}}$ for the best pairing.

We find the center of energy of the kaon decay at the CsI calorimeter plane by weighting the position of each photon with its energy. The x and y components of the center of energy are

$$ x_{\text{coe}} \equiv \frac{\sum x_i E_i}{\sum E_i}, \qquad y_{\text{coe}} \equiv \frac{\sum y_i E_i}{\sum E_i}, \tag{8} $$

where the sums are over all four photons. The center of energy is the point at which the kaon would have intercepted the plane of the CsI calorimeter if it had not decayed, so we can calculate the (x, y) position of the decay vertex by assuming it lies on the line between the target and the center of energy. The x coordinate of the kaon decay vertex is used to determine whether the kaon came from the regenerator or the vacuum beam.

The $\pi^0 \pi^0$ invariant mass is calculated from the coordinates of the kaon decay vertex and the four photon positions and energies. The kaon energy is calculated as the sum of the four photon energies.

3. $K \rightarrow \pi^0 \pi^0$ selection

The $K \rightarrow \pi^0 \pi^0$ event selection begins with three levels of trigger requirements during data taking. The $K \rightarrow \pi^0 \pi^0$ level 1 trigger requires that the total energy in the CsI calorimeter be greater than 30 GeV. The inefficiency in this trigger is studied using $K \rightarrow \pi^+ \pi^- \pi^0$ decays from the $K \rightarrow \pi^+ \pi^-$ trigger; the inefficiency at a given energy E_{total} is the ratio of events with energy greater than E_{total} for which the level 1 trigger bit is not set to the total number of events with energy greater than E_{total}. We find inefficiencies ranging from $(0.5\text{–}1.6) \times 10^{-4}$ in the 40–160 GeV energy range used for the analysis. The impact of this inefficiency is slightly different in the vacuum and regenerator beams because of small differences in the energy distributions. The resulting bias in $\text{Re}(\epsilon'/\epsilon)$ is less than 0.02×10^{-4}, which we assign as a systematic error.

The level 2 trigger requirement is based on the "hardware cluster counter" [26]. The inefficiency in this trigger is measured using $K_L \rightarrow \pi^0 \pi^0 \pi^0$ decays from a trigger that has no level 2 requirement. We reconstruct the $K_L \rightarrow \pi^0 \pi^0 \pi^0$ decays without any requirement on the hardware cluster counter; the level 2 inefficiency is the ratio of the number of events that do not meet the hardware cluster counter requirement to the total number of events found in the offline reconstruction. The bias in $\text{Re}(\epsilon'/\epsilon)$ produced by this inefficiency is determined using $K \rightarrow \pi^0 \pi^0$ MC. The inefficiency is simulated to within 10% by the Monte Carlo, so we take 10% of the measured bias as the systematic uncertainty in $\text{Re}(\epsilon'/\epsilon)$. The total uncertainty in $\text{Re}(\epsilon'/\epsilon)$ associated with the level 2 trigger is 0.19×10^{-4}.

The inefficiency of the level 3 $K \rightarrow \pi^0 \pi^0$ trigger is studied using random accepts, a prescaled subset of the $K \rightarrow \pi^0 \pi^0$ trigger that has no level 3 requirement. We find no statistically significant bias in $\text{Re}(\epsilon'/\epsilon)$ and quote an uncertainty of 0.07×10^{-4} in $\text{Re}(\epsilon'/\epsilon)$ based on the statistical precision of the bias measurement.

The offline selection criteria for the $K \rightarrow \pi^0 \pi^0$ sample are designed to select events that are cleanly reconstructed, to suppress background, and to select kinematic and fiducial regions appropriate for the KTeV detector. We evaluate the systematic uncertainty associated with each of the following requirements by loosening or removing the cut and evaluating the change in $\text{Re}(\epsilon'/\epsilon)$.

The energy of each CsI calorimeter cluster is required to be greater than 3 GeV because the clustering corrections and MC simulation are not reliable at very low energies. The minimum distance between the reconstructed positions of CsI calorimeter clusters is required to be greater than 7.5 cm because it is difficult to separate the energy deposits in two very close clusters. Clusters very near

the beam holes are not as well-reconstructed because of energy leakage across the beam holes and multiple overlapping or nearby clusters. In KTeV03, the inner CsI aperture was defined by the collar anti (CA) detector; we now remove events with clusters having a seed crystal in the first ring of crystals around the beam holes. We do not find any systematic variation of $\text{Re}(\epsilon'/\epsilon)$ with these requirements.

The variable describing the quality of the photon pairing, $\chi^2_{\pi^0}$ [Eq. (7)], is required to be less than 50. This is a rather loose cut since more than 99% of $K \to \pi^0\pi^0$ events passing all other cuts have $\chi^2_{\pi^0}$ values below 10. The primary purpose of this cut is to reduce background from $K_L \to \pi^0\pi^0\pi^0$ events in which two of the photons escape the detector; in this case it is likely that the missing photons come from different pions causing the remaining photons to be paired incorrectly. The systematic uncertainty in $\text{Re}(\epsilon'/\epsilon)$ associated with this requirement is 0.14×10^{-4}.

The "shape chi-squared" variable χ^2_γ is a measure of how well the transverse energy distribution of each CsI calorimeter cluster matches the expected distribution for a photon. This variable, which is not a true chi-squared because of correlations that are not considered, is calculated by comparing the transverse energy distribution of each cluster to the transverse energy maps described in Sec. III C 1. The maximum value of χ^2_γ for each event is required to be less than 48. The purpose of this cut is to remove background from $K_L \to \pi^0\pi^0\pi^0$ events in which two or more photons overlap in the CsI calorimeter and are reconstructed as a single cluster. In these cases the transverse distribution of energy would tend to be different from that of a single photon cluster. The systematic uncertainty in $\text{Re}(\epsilon'/\epsilon)$ associated with the shape chi-squared requirement is 0.15×10^{-4}.

We make a number of cuts on the veto detectors to reduce background. We also use the calorimeter, spectrometer, and trigger hodoscope as veto detectors by cutting on extra clusters, tracks, and hits. There is no systematic uncertainty associated with these requirements.

In the $K \to \pi^+\pi^-$ analysis we use p_T^2 to remove events in which the kaon scatters in the collimator or the regenerator. This variable is not available for $K \to \pi^0\pi^0$ decays since we do not measure the photon angles, so we use the "ring number" variable to reject scattered kaon decays. The ring number is calculated using the center of energy of the reconstructed clusters and is defined as

$$\text{ring} = 40\,000 \times \text{Max}(\Delta x^2_{\text{coe}}, \Delta y^2_{\text{coe}}), \qquad (9)$$

where Δx_{coe} and Δy_{coe} are the distances from the center of energy to the center of the closest beam hole. A change of $\Delta \text{ring} = 1$ corresponds to an incremental area of 1 cm^2 centered on the beam hole. Events with a ring number less than 81 cm^2 should be from kaons decaying inside one of

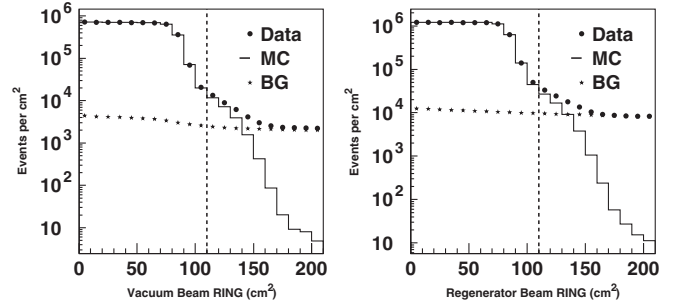FIG. 11. $K \to \pi^0\pi^0$ ring distributions for data and signal MC in the vacuum (left) and regenerator (right) beams. The dashed line indicates our cut.

the two beams. Figure 11 shows the ring number distributions for both beams for the data and Monte Carlo. The ring number is required to be less than 110 cm^2; the systematic uncertainty in $\text{Re}(\epsilon'/\epsilon)$ associated with this requirement is 0.27×10^{-4}.

The limiting apertures for $K \to \pi^0\pi^0$ events are the CsI calorimeter inner aperture at the beam holes, the CsI calorimeter outer aperture, the upstream edge in each beam, and an effective inner aperture resulting from the 7.5 cm photon separation requirement at the CsI calorimeter. The CsI calorimeter inner and outer apertures are

TABLE II. Summary of systematic uncertainties in $\text{Re}(\epsilon'/\epsilon)$ from the $K \to \pi^0\pi^0$ analysis. The final systematic uncertainties for the combined data set are listed in the column labeled "Full." For those uncertainties that are also evaluated separately in the three years, the individual uncertainties are shown to facilitate comparison with the KTeV03 result.

| Source | Error on $\text{Re}(\epsilon'/\epsilon)$ ($\times 10^{-4}$) | | | | |
| | | Current result | | | |
	KTeV03 result	1996	1997	1999	Full
L1 trigger	0.10	0.01	0.01	0.03	0.02
L2 trigger	0.13	0.20	0.12	0.23	0.19
L3 trigger	0.08	0.20	0.04	0.05	0.07
Ring number	0.24		0.27		0.27
Pairing χ^2	0.20		0.14		0.14
Shape χ^2	0.20		0.15		0.15
Energy nonlinearity	0.66	0.10	0.10	0.20	0.15
Energy scale	1.27	0.45	0.82	0.59	0.65
Position reconstruction	0.35		0.35		0.35
Background	1.07	1.14	1.06		1.07
CsI inner aperture	0.42		0.42		0.42
MA aperture	0.18		0.18		0.18
Reg edge	0.04		0.04		0.04
CsI size	0.15		0.15		0.15
Acceptance	0.39		0.48		0.48
MC statistics	0.40	0.75	0.37	0.41	0.25
Total	2.01	1.69	1.63	1.56	1.55
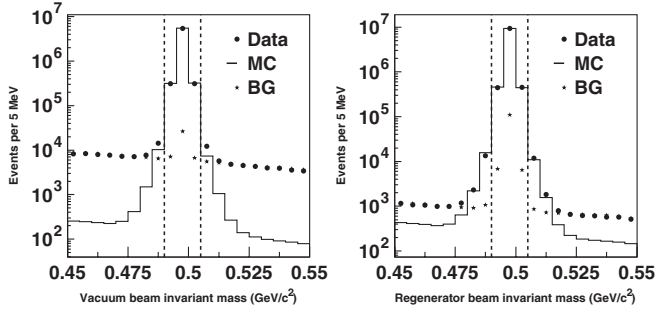
FIG. 12. $K \rightarrow \pi^0 \pi^0$ $m_{\pi^0 \pi^0}$ distributions for data and signal MC in the vacuum (left) and regenerator (right) beams. The dashed lines indicate our cuts.

defined by rejecting events in which a photon hits the innermost or outermost ring of CsI crystals. The upstream aperture in the vacuum beam is defined by the mask anti and the upstream aperture in the regenerator beam is defined by the lead module at the downstream edge of the regenerator. The systematic errors associated with the precision of these apertures are discussed in the KTeV03 paper [20] and have not changed; the individual values are listed in Table II. The total systematic uncertainty in Re(ϵ'/ϵ) associated with limiting apertures in the $K \rightarrow \pi^0 \pi^0$ analysis is 0.48×10^{-4}.

Figure 12 shows the reconstructed kaon mass distributions for both beams for the data and Monte Carlo. The mass is required to be $490 \text{ MeV}/c^2 < m\pi^0\pi^0 < 505 \text{ MeV}/c^2$. The sidebands of the $m\pi^0\pi^0$ distribution are almost exclusively $K_L \rightarrow \pi^0\pi^0\pi^0$ background, with a small contribution from events in which the photons have been mispaired. The peaking background at the kaon mass is from decays of kaons which scattered with a nonzero angle in the regenerator and the defining collimators. More details on the background are given in Sec. III D.

4. Energy systematics

The reconstruction of $K \rightarrow \pi^0 \pi^0$ decays depends entirely on the reconstruction of energies and positions of photon showers in the CsI calorimeter. Reconstructed quantities may depend upon the absolute energy scale or the energy linearity of the CsI calorimeter. We apply corrections that match the energy scale between the data and Monte Carlo, and we assign systematic uncertainties based on any disagreement in either absolute energy scale or energy linearity between the data and Monte Carlo. The procedures for matching the energy scale and evaluating the energy systematics are described in this section.

The energy scale of the CsI calorimeter is set by the electron calibration, but there is a small, residual difference in energy scale between the data and Monte Carlo for $K \rightarrow \pi^0 \pi^0$ events. This difference is removed by adjusting the energy scale in the data such that the sharp edge in the z-vertex distribution at the regenerator matches between the data and Monte Carlo, as shown in Fig. 13. The
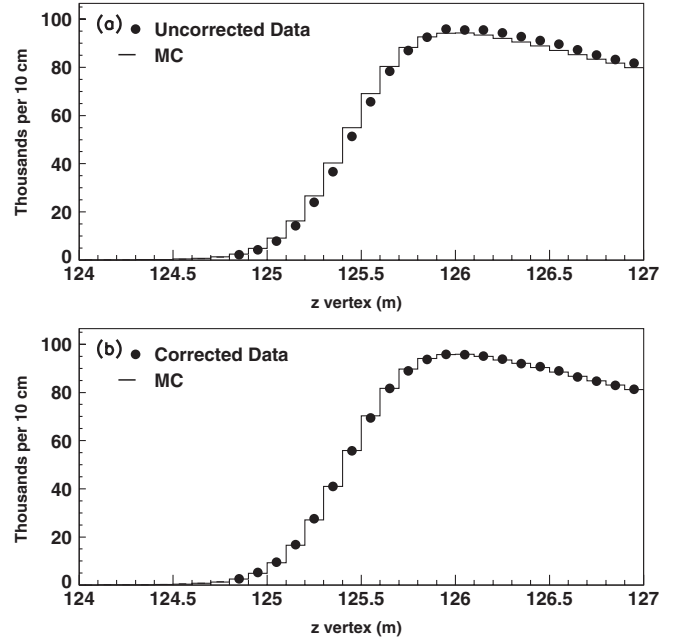

FIG. 13. Regenerator beam $K \rightarrow \pi^0 \pi^0$ z-vertex distribution near the regenerator for 1999 data and Monte Carlo. (a) Uncorrected data. (b) Data with the energy scale correction applied.

correction is determined by sliding finely binned $K \rightarrow \pi^0 \pi^0$ data and Monte Carlo z-vertex distributions in the regenerator beam past each other and using the Kolmogorov-Smirnov test to determine how much the data must be adjusted to best match the MC. The correction is binned in kaon energy in the same 10 GeV energy bins that are used to extract our results (see Sec. IV B). The same correction is applied to each cluster in an event.

The final energy scale adjustment is shown as a function of kaon energy in Fig. 14. The average size of the z-vertex shift is ~ 2.5 cm. This corresponds to an average energy correction of $\sim 0.04\%$, compared to $\sim 0.1\%$ in KTeV03. As a result of improvements to the simulation and reconstruction of clusters, the required energy scale adjustment in the
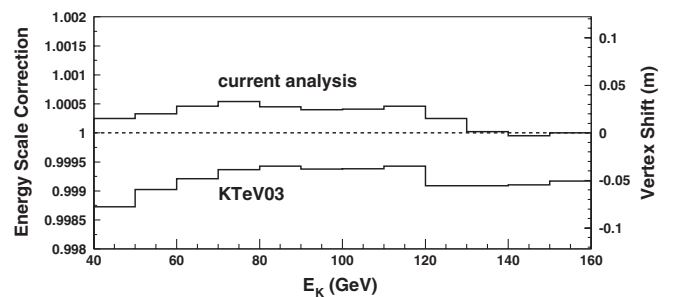

FIG. 14. Change in the final energy scale adjustment relative to KTeV03. The dashed line represents no data-MC mismatch. The y axis on the right side of the plot shows the data-MC z-vertex shift in meters.

current analysis is smaller and less dependent on kaon energy than in the KTeV03 analysis.

This final energy scale adjustment ensures that the energy scale matches between the data and MC at the regenerator edge, but we must check whether the data and MC energy scales remain matched for the full length of the decay volume. Any nonlinearity would result in different effective energy scales at different decay points because of the correlation between the z-vertex and kaon energy distributions. We check the energy scale at the downstream end of the decay region by studying the z-vertex distribution of $\pi^0\pi^0$ pairs produced by hadronic interactions in the vacuum window and other downstream detector elements in the data and MC. To verify that this type of production has a comparable energy scale to $K \to \pi^0\pi^0$, we also study the z-vertex distribution of hadronic $\pi^0\pi^0$ pairs produced in the regenerator. The z-vertex distribution of regenerator hadronic events is Gaussian while the distribution of downstream events is more complicated, as described below. The methods for making the data-MC comparison in each case are described in the following paragraphs.

We compare the Gaussian z-vertex distributions of hadronically produced regenerator events between the data and MC by sliding the distributions past each other and using the chi-squared test. The average data-MC difference is plotted in Fig. 15; we find no significant data-MC mismatch in this sample.

For the downstream hadronic events, we consider interactions in four separate detector volumes: the vacuum window, the upstream drift chamber, and the two helium bags surrounding the drift chamber. The production of $\pi^0\pi^0$ pairs in each of these volumes is simulated separately; a fit is used to determine the relative contribution of each material and to find the difference between the data and MC z-vertex distributions. The fit is performed separately for the 1996, 1997, and 1999 data samples. Figure 16 shows the z-vertex distributions of downstream hadronic $\pi^0\pi^0$ pairs for 1999 data and MC, before and after the Monte Carlo data are shifted by the measured 1.06 cm data-MC difference. The z shifts measured for each year are plotted in Fig. 15.

To convert these shifts to an uncertainty in $\mathrm{Re}(\epsilon'/\epsilon)$, we consider a linearly varying energy scale distortion such that no adjustment is made at the regenerator edge and the z shift at the vacuum window is that measured by the hadronic downstream sample. This distortion is shown by the shaded region in Fig. 15. We rule out energy scale distortions that vary nonlinearly as a function of the z vertex because they introduce data-MC discrepancies in other distributions. The systematic error on $\mathrm{Re}(\epsilon'/\epsilon)$ due to uncertainties in the $K \to \pi^0\pi^0$ energy scale is 0.65×10^{-4}.

To evaluate the effect of energy nonlinearities on the reconstruction, we study the way the reconstructed kaon mass, which does not depend on the absolute energy scale, varies with reconstructed kaon energy, kaon z vertex, minimum cluster separation, and incident photon angle.
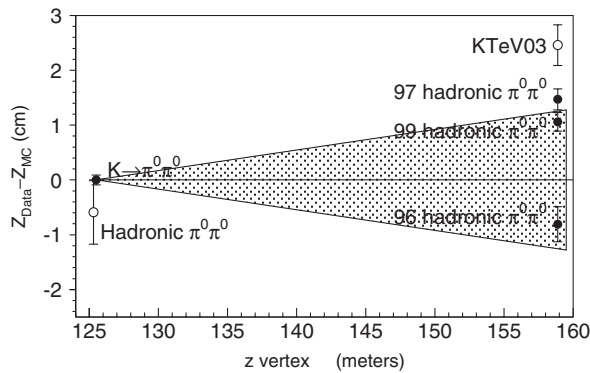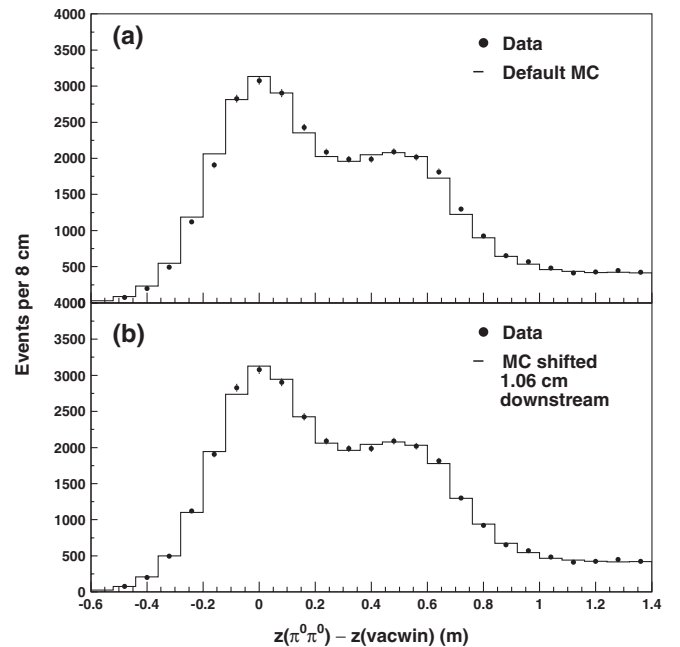

FIG. 15. Energy scale tests at the regenerator and vacuum window. The difference between the reconstructed z positions for the data and MC is plotted for $K \to \pi^0\pi^0$ events and for hadronically produced $\pi^0\pi^0$ pairs at the regenerator and the downstream detector elements. The solid point at the regenerator edge is the $K \to \pi^0\pi^0$ sample; there is no difference between the data and MC by construction. The open point at the regenerator edge is the average shift of the hadronic regenerator samples for all three data sets. The points at the vacuum window are the shifts for the downstream hadronic events for each data set separately. The shaded region shows the range of data-MC shifts covered by the total systematic uncertainty from the energy scale. For reference, the data-MC shift at the vacuum window from KTeV03 is also plotted.

FIG. 16. z-vertex distributions of $\pi^0\pi^0$ pairs produced hadronically in downstream detector elements for 1999 data and MC. (a) Data (dots) and nominal MC (histogram). (b) Data (dots) and MC that is shifted 1.06 cm downstream to match the data (histogram).
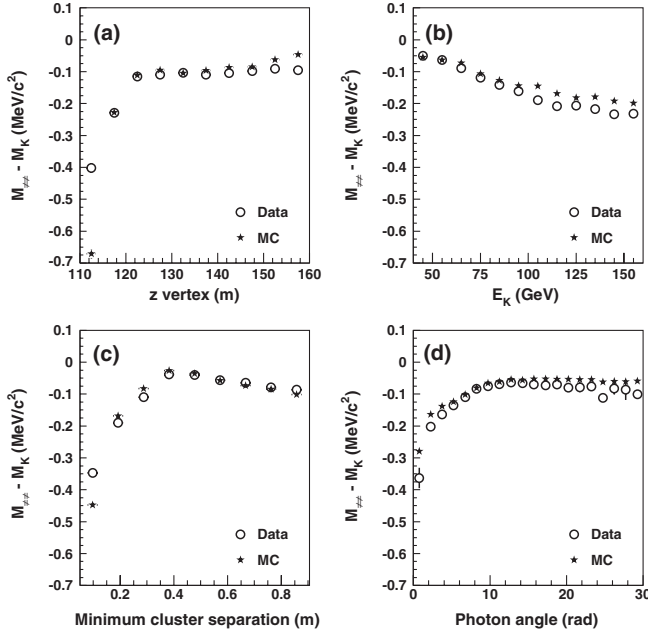
FIG. 17. Comparisons of the reconstructed kaon mass vs (a) z vertex, (b) kaon energy, (c) minimum cluster separation, and (d) photon angle for 1999 data (circles) and MC (stars). The values plotted are the difference between the reconstructed kaon mass for each bin and the PDG kaon mass.

Data-MC comparisons for these distributions for the 1999 data sample are shown in Fig. 17. To measure any bias resulting from the nonlinearities that cause the small data-MC differences seen in these distributions, we investigate adjustments to the cluster energies that improve the agreement between the data and MC in the plot of reconstructed kaon mass vs kaon energy. We find that a 0.1%/100 GeV distortion produces the best data-MC agreement for the 1997 and 1999 data sets. Figure 18 shows the improvement in data-MC agreement with this distortion applied to 1999 data. The 1996 data set has slightly larger nonlinearities; we find that a 0.3%/100 GeV distortion produces the best data-MC agreement for this data set. The data-MC agreement in the reconstructed kaon mass as a function of kaon energy has been significantly improved compared to KTeV03, where a 0.7%/100 GeV distortion was required.
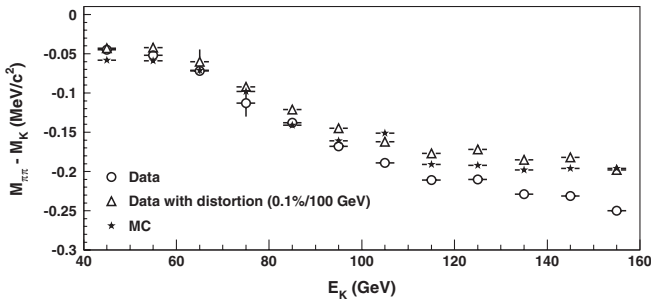

FIG. 18. Effect of 0.1%/100 GeV distortion on M_K vs E_K for 1999 data. The values plotted are the difference between the reconstructed kaon mass for each bin and the PDG kaon mass.

To evaluate the systematic error associated with these nonlinearities, we apply the distortions to the data and find that $\mathrm{Re}(\epsilon'/\epsilon)$ changes by less than 0.2×10^{-4} for all three data sets. Properly weighting the three data sets, we find that the systematic uncertainty on $\mathrm{Re}(\epsilon'/\epsilon)$ due to energy nonlinearities is 0.15×10^{-4}.

The systematic uncertainties in $\mathrm{Re}(\epsilon'/\epsilon)$ from the $K \rightarrow \pi^0\pi^0$ analysis are summarized in Table II. The $K \rightarrow \pi^0\pi^0$ analysis contributes an uncertainty in $\mathrm{Re}(\epsilon'/\epsilon)$ of 1.55×10^{-4}, which is reduced by $\sim 23\%$ from KTeV03.

D. Background and systematics

The background to the $K \rightarrow \pi\pi$ signal modes is simulated using the Monte Carlo, normalized to data outside the signal region, and subtracted. There are two categories of background in this analysis: scattered $K \rightarrow \pi\pi$ events and non-$\pi\pi$ background. We use decays from coherently regenerated kaons only; any kaons that scatter with a nonzero angle in the regenerator are treated as a background. This regenerator scattering background and the background from kaons that scatter in the defining collimators have the same momentum and p_T^2 distributions for both $K \rightarrow \pi^+\pi^-$ and $K \rightarrow \pi^0\pi^0$ decays. This background can be identified using the reconstructed transverse momentum of the decay products in the charged decay mode. Therefore, the scattering background is small in the charged mode, and we may use $K \rightarrow \pi^+\pi^-$ decays to tune the simulation of scattering background on which we must rely in the neutral mode.

The non-$\pi\pi$ background is present because of misidentification of high branching-ratio decay modes. The background to $K \rightarrow \pi^+\pi^-$ decays comes from $K_L \rightarrow \pi^\pm e^\mp \nu$ and $K_L \rightarrow \pi^\pm \mu^\mp \nu$ decay modes. The background to $K \rightarrow \pi^0\pi^0$ decays comes from $K_L \rightarrow \pi^0\pi^0\pi^0$ decays and hadronic interactions in the regenerator. The background estimation procedure and the associated systematic uncertainties are described in detail in [20].

There is only one significant change to the background estimation procedure since KTeV03. Hadronic production of K^* and Δ resonances via $K_L + N \rightarrow K_S^* + X$ and $n + N \rightarrow \Delta + X$ is now included in the $K \rightarrow \pi^+\pi^-$ regenerator beam background analysis; these background sources were not considered in the KTeV03 analysis. The incident neutron spectrum is assumed to be the same as that of the Λ baryon, which is measured in the data. For K_S^* decays, both $K^\pm \pi^\mp$ and $\pi^0 K_S$, $K_S \rightarrow \pi^+\pi^-$ modes are simulated. The $K_S^* \rightarrow \pi^0 K_S$ background is normalized using the transverse momentum sideband in the regenerator beam. The $K_S^* \rightarrow K^\pm \pi^\mp$ and $\Delta \rightarrow p^\pm \pi^\mp$ decays are normalized using mass sidebands in the regenerator beam reconstructed assuming the vertex is located at the regenerator edge. These two modes are separated using the momentum asymmetry distribution of the secondary particles. The hadronic K^* and Δ background samples have negligible contributions to the signal region after all

TABLE III. Summary of $K \to \pi^+ \pi^-$ background levels.

Source	Vacuum beam		Regenerator beam	
	1997	1999	1997	1999
Regenerator scattering	$\cdots$	$\cdots$	0.073%	0.075%
Collimator scattering	0.009%	0.008%	0.009%	0.008%
$K_L \to \pi^{\pm} e^{\mp} \nu$	0.032%	0.032%	0.001%	0.001%
$K_L \to \pi^{\pm} \mu^{\mp} \nu$	0.034%	0.030%	0.001%	0.001%
Total background	0.074%	0.070%	0.083%	0.085%

TABLE IV. Summary of $K \to \pi^0 \pi^0$ background levels. Note that photon mispairing is not subtracted from the data and is not included in the total background sum.

Source	Vacuum beam			Regenerator beam		
	1996	1997	1999	1996	1997	1999
Regenerator scattering	0.288%	0.260%	0.258%	1.107%	1.092%	1.081%
Collimator scattering	0.102%	0.122%	0.120%	0.081%	0.093%	0.091%
$K_L \to \pi^0 \pi^0 \pi^0$	0.444%	0.220%	0.301%	0.015%	0.006%	0.012%
Photon mispairing	0.007%	0.007%	0.008%	0.007%	0.008%	0.007%
Hadronic production	0.002%	0.001%	$\cdots$	0.007%	0.007%	0.007%
Total background	0.835%	0.603%	0.678%	1.209%	1.197%	1.190%

selection cuts, but including them improves the description of mass and p_T sidebands.

The background levels in $K \to \pi^+ \pi^-$ are illustrated in Figs. 8 and 9, and the background to $K \to \pi^0 \pi^0$ may be seen in Figs. 11 and 12. Background contributes less than 0.1% of $K \to \pi^+ \pi^-$ events and about 1% of $K \to \pi^0 \pi^0$ events. Tables III and IV contain summaries of all the background fractions for each data set. There are some variations in background levels among the years due to differences in trigger and veto requirements. The systematic uncertainty in $\mathrm{Re}(\epsilon'/\epsilon)$ due to background is 0.20×10^{-4} from $K \to \pi^+ \pi^-$ and 1.07×10^{-4} from $K \to \pi^0 \pi^0$.

E. Data summary

The numbers of events collected in each beam are summarized in Table V. After all event selection requirements are applied and background is subtracted, we have a total of 25×10^6 vacuum beam $K \to \pi^+ \pi^-$ decays and 6×10^6 vacuum beam $K \to \pi^0 \pi^0$ decays.

IV. ACCEPTANCE AND FITTING

A. Acceptance correction and systematics

We use the Monte Carlo simulation to estimate the acceptance of the detector in momentum and z-vertex

TABLE V. Summary of event totals after all selection criteria and background subtraction.

	Vacuum beam	Regenerator beam
$K \to \pi^+ \pi^-$	25 107 242	43 674 208
$K \to \pi^0 \pi^0$	5 968 198	10 180 175

bins in each beam. We evaluate the quality of this simulation by comparing z-vertex distributions in the vacuum beam between the data and Monte Carlo. To account for small differences in the energy spectrum between the data and Monte Carlo, we reweight the distributions, using the same 10 GeV/c momentum bins used by the fitter (see Sec. IV B), by adjusting the number of MC events in each bin so that the data and MC kaon momentum distributions agree. We fit the data-MC ratio of z-vertex distributions to a line and call the slope of this line, s, the acceptance "z slope." We use this z slope to evaluate the systematic error on $\mathrm{Re}(\epsilon'/\epsilon)$.

A z slope affects the value of $\mathrm{Re}(\epsilon'/\epsilon)$ by producing a bias between the regenerator and vacuum beams because of the different z-vertex distributions in the two beams. A good approximation of the bias on $\mathrm{Re}(\epsilon'/\epsilon)$ is $s\Delta z/6$, where Δz is the difference of the mean z values for the vacuum and regenerator beam z-vertex distributions. The factor of 6 converts the bias on the vacuum-regenerator beam ratio to a bias on $\mathrm{Re}(\epsilon'/\epsilon)$. The values of Δz are 5.6 m for the $K \to \pi^+ \pi^-$ sample and 7.2 m for the $K \to \pi^0 \pi^0$ sample. We use the measured bias on $\mathrm{Re}(\epsilon'/\epsilon)$ and the statistical error on that measurement to assign a systematic uncertainty in $\mathrm{Re}(\epsilon'/\epsilon)$.

The z slopes for the full data set are shown in Fig. 19. We use the 25×10^6 vacuum beam $K \to \pi^+ \pi^-$ decays to measure the z slope in the charged decay mode. The uncertainty in $\mathrm{Re}(\epsilon'/\epsilon)$ associated with this z slope is 0.41×10^{-4}. We assign an additional uncertainty of 0.40×10^{-4} based on a $\mathrm{Re}(\epsilon'/\epsilon)$ fit which excludes $K \to \pi^+ \pi^-$ decays from the region upstream of the MA. This region is very sensitive to the value of the MA aperture cut (see Sec. III B), and, since it lies upstream of
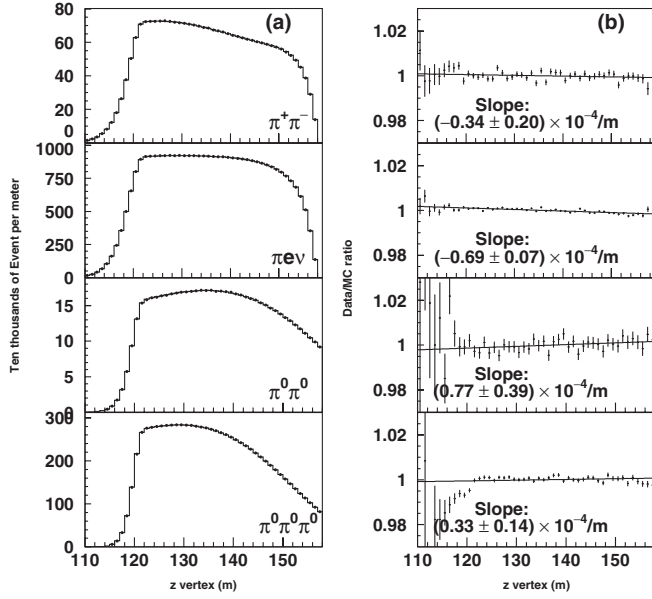
FIG. 19.   (a) Comparison of the vacuum beam z distributions for the data (dots) and MC (histogram). (b) The data-to-MC ratios are fit to a line, and the z slopes (see text) are shown. All distributions are for the full data sample used in this analysis.

the regenerator edge, there are no regenerator beam decays to compensate for this dependence. Combining these two uncertainties, the systematic uncertainty in $\text{Re}(\epsilon'/\epsilon)$ associated with the acceptance correction is 0.57×10^{-4}.

We also measure the data-MC z slope in the high statistics $K_L \to \pi^{\pm} e^{\mp} \nu$ decay mode and find a slope that is similar in magnitude to the systematic uncertainty from $K \to \pi^+ \pi^-$. We do not use the $K_L \to \pi^{\pm} e^{\mp} \nu$ z slope to set the systematic error because it is sensitive to different detector effects and has different particle types in the final state than $K \to \pi^+ \pi^-$.

We use 88×10^6 $K_L \to \pi^0 \pi^0 \pi^0$ decays to measure the z slope in the neutral decay mode. This mode has the same type of particles in the final state as $K \to \pi^0 \pi^0$, and it is more sensitive than $\pi^0 \pi^0$ to potential problems in the reconstruction due to close clusters, energy leakage at the CsI calorimeter edges, and low photon energies. We assign an uncertainty on $\text{Re}(\epsilon'/\epsilon)$ from the neutral mode acceptance of 0.48×10^{-4} based on the $K_L \to \pi^0 \pi^0 \pi^0$ z slope. We also measure the z slope in $K \to \pi^0 \pi^0$ decays and find that the results are consistent with those from $K_L \to \pi^0 \pi^0 \pi^0$ decays. There is no significant change in $\text{Re}(\epsilon'/\epsilon)$ when the region upstream of the MA is excluded in the neutral mode, so no additional systematic uncertainty is required.

B. Fitting and systematics

The value of $\text{Re}(\epsilon'/\epsilon)$ and other kaon parameters Δm, τ_S, ϕ_{ϵ}, and $\text{Im}(\epsilon'/\epsilon)$ are determined using a fitting program. The fitting procedure is to minimize χ^2 between the

background subtracted data and a prediction function. The prediction function uses the detector acceptance determined with the Monte Carlo simulation. The fits are performed in 10 GeV/c kaon momentum bins. There is no z binning to determine $\text{Re}(\epsilon'/\epsilon)$, while a z-binned fit is performed to measure the other kaon parameters. Uncertainties from the fitting procedure are mainly related to regenerator properties and the dependence of the result on external parameters.

Neglecting the contribution from K_S produced at the target (called target K_S), the number of $K \to \pi\pi$ events in the vacuum beam for a given p, z is

$$N^{\pi\pi}(p, z) \sim \mathcal{F}(p)|\eta|^2 \exp\left(-\frac{t}{\tau_L}\right), \qquad (10)$$

where $t = (z - z_{\text{reg}})m_K/p$ is the measured proper time relative to decays at the regenerator edge, $\eta = \eta_{+-} = \epsilon + \epsilon'$ ($\eta = \eta_{00} = \epsilon - 2\epsilon'$) for charged (neutral) decays, and $\mathcal{F}(p)$ is the kaon flux. The fitting program includes the contribution of target K_S by using a phenomenological model for $K^0/\bar{K}^0$ production at the target and propagating the kaon states up to the decay volume. The model of target-K_S production is checked by floating the $K^0/\bar{K}^0$ flux ratio in the fit. The fitted fraction of target K_S deviates from the model by $(2.5 \pm 1.6)\%$. The associated systematic uncertainty in $\text{Re}(\epsilon'/\epsilon)$ is $\pm 0.12 \times 10^{-4}$.

The number of events in the regenerator beam is

$$
\begin{aligned}
N^{\pi\pi}(p, z) \sim \mathcal{F}(p) T_{\text{reg}}(p) \Bigg[& |\rho(p)|^2 \exp\left(-\frac{t}{\tau_S}\right) \\
& + |\eta|^2 \exp\left(-\frac{t}{\tau_L}\right) + 2|\rho(p)||\eta| \\
& \times \cos(\Delta m t + \phi_{\rho}(p) - \phi_{\eta}) \exp\left(-\frac{t}{\tau_{\text{ave}}}\right) \Bigg],
\end{aligned}
$$
(11)

where $\rho(p)$ is the momentum-dependent coherent regeneration amplitude, $\phi_{\rho}(p) = \arg(\rho)$, $1/\tau_{\text{ave}} = (1/\tau_S + 1/\tau_L)/2$, and $T_{\text{reg}}(p)$ is the relative kaon flux transmission in the regenerator beam. The prediction function accounts for decays inside the regenerator by using the effective regenerator edge [Fig. 3(b)] as the start of the decay region.

The parameters from Eqs. (10) and (11) are determined as discussed below. The kaon flux $\mathcal{F}(p)$ is a free parameter for each of the twelve 10 GeV/c momentum bins. Separate kaon fluxes are allowed for charged and neutral decays to account for slight differences in the data samples, so there are a total of $12 \times 2 = 24$ free fit parameters to describe the kaon flux. The flux ratio of decays in the vacuum and regenerator beams is, however, the same in both charged and neutral decay modes. The 1996 $K \to \pi^0 \pi^0$ data have no corresponding $K \to \pi^+ \pi^-$ data, so it is possible that there could be small differences in the flux ratio between the two years which do not cancel in the fit.

We assign an uncertainty in $\text{Re}(\epsilon'/\epsilon)$ of $\pm 0.03 \times 10^{-4}$ from this possibility, following [18].

The relative kaon flux attenuation in the regenerator beam, T_{reg}, results from the shadow absorber and the regenerator itself. The attenuation is measured directly from the data by comparing the rate of $K_L \rightarrow \pi^+ \pi^- \pi^0$ decays in the vacuum (N_{vac}^{+-0}) and regenerator (N_{reg}^{+-0}) beams. As mentioned earlier, a dedicated trigger was introduced in 1999 to improve the statistical precision of this measurement; the improved measurement is applicable for all years of data taking. The attenuation is found to be a linear function of p for a kaon momentum range of 40–160 GeV/c as shown in Fig. 20. For the 61.5 GeV/c average momentum of $K_L \rightarrow \pi^+ \pi^- \pi^0$ decays, the transmission is $T_0 = (7.771 \pm 0.004)\%$. The slope of the momentum dependence is $\alpha_T = (-3.5 \pm 0.2) \times 10^{-5}$ c/GeV where the errors represent total experimental uncertainties. The uncertainty on the momentum dependence of the regenerator attenuation corresponds to a 0.08×10^{-4} uncertainty in $\text{Re}(\epsilon'/\epsilon)$.

The regeneration amplitude ρ is related to the difference between the forward kaon-nucleon scattering amplitudes for K^0, $f(0)$ and $\bar{K}^0$, $\bar{f}(0)$ [27]:

$$f_- = \hbar \frac{f(0) - \bar{f}(0)}{p}. \quad (12)$$

The KTeV regenerator is composed mostly of plastic scintillator with two thin lead plates in the last module [see Fig. 3(a)]. The dominant source for regeneration is forward scattering in carbon with small additional contributions from hydrogen and lead. The regeneration in hydrogen and lead is fixed in the fit while the parameters describing carbon regeneration are allowed to float.

For an isoscalar target (C_{12}) and high kaon momentum, f_- can be approximated by a single Regge trajectory [28] and the magnitude of f_- varies with kaon momentum as a power law, $|f_-(p)| \sim p^\alpha$. The analyticity of the forward

TABLE VI. Summary of systematic uncertainties in $\text{Re}(\epsilon'/\epsilon)$ associated with fitting.

Source	Error on $\text{Re}(\epsilon'/\epsilon)$ ($\times 10^{-4}$)
Regenerator transmission	0.08
Target K_S	0.12
Δm and τ_S	0.11
Regenerator screening	0.24
ϕ_ρ (analyticity)	0.07
1996 K_S/K_L flux ratio	0.03
τ_L	0.01
Total	0.31

scattering amplitude relates the magnitude of $f_-(p)$ and its phase, $\arg(f_-)$. The magnitude of $|f_-|$ at $p = 70$ GeV/c and the power law α are the two free parameters describing regeneration in the fit. We estimate the systematic error from the analyticity assumption by allowing ϕ_ρ to deviate $0.25°$ from analyticity; the associated uncertainty in $\text{Re}(\epsilon'/\epsilon)$ is 0.07×10^{-4}.

For scattering off complex nuclei, the effects of nuclear screening corrections are important and the regeneration amplitude cannot be described by a single power law. We vary the screening models in the fit and find that the associated $\text{Re}(\epsilon'/\epsilon)$ uncertainty is 0.24×10^{-4}. More details on the screening corrections and the analyticity relation for the scattering amplitude are given in the appendix

The K_L lifetime τ_L is taken from [29]; the uncertainty in $\text{Re}(\epsilon'/\epsilon)$ due to the uncertainty in this measurement is 0.01×10^{-4}. The values of Δm and τ_S are fixed to our measurements [Eq. (21)] for the $\text{Re}(\epsilon'/\epsilon)$ fit and are floated in the z-binned fit. The uncertainty in $\text{Re}(\epsilon'/\epsilon)$ due to the values of Δm and τ_S used in the fit is 0.11×10^{-4}.

The systematic uncertainties in $\text{Re}(\epsilon'/\epsilon)$ associated with fitting are summarized in Table VI. The total systematic uncertainty in $\text{Re}(\epsilon'/\epsilon)$ from fitting is 0.31×10^{-4}.

V. RESULTS

A. Measurement of $\text{Re}(\epsilon'/\epsilon)$

In the KTeV fit for $\text{Re}(\epsilon'/\epsilon)$, the inputs are the observed number of $K \rightarrow \pi^+ \pi^-$ and $K \rightarrow \pi^0 \pi^0$ decays in each of twelve 10 GeV/c momentum bins. The kaon fluxes for $K \rightarrow \pi^+ \pi^-$ and $K \rightarrow \pi^0 \pi^0$ in each momentum bin, the regeneration parameters, and $\text{Re}(\epsilon'/\epsilon)$ are free parameters. *CPT* symmetry is assumed by setting the phases ϕ_{+-} and ϕ_{00} equal to the superweak phase. The final KTeV result is

$$\text{Re}(\epsilon'/\epsilon) = [19.2 \pm 1.1(\text{stat}) \pm 1.8(\text{syst})] \times 10^{-4}$$

$$= [19.2 \pm 2.1] \times 10^{-4}. \quad (13)$$

The fit χ^2 is $\chi^2/\nu = 22.9/21$. The systematic uncertainties in $\text{Re}(\epsilon'/\epsilon)$ are summarized in Table VII. This result corresponds to a particle-antiparticle partial decay rate asymmetry of
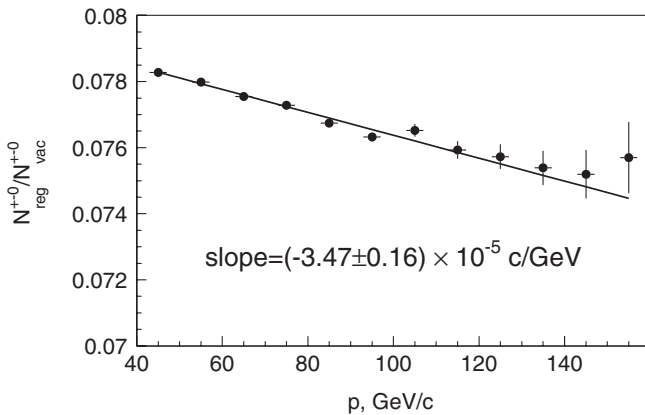

FIG. 20. Ratio of $K_L \rightarrow \pi^+ \pi^- \pi^0$ decay rates in the regenerator to vacuum beam as a function of a kaon momentum. The uncertainty on the slope is statistical uncertainty of the measurement.

slope=(-3.47±0.16) × 10⁻⁵ c/GeV

TABLE VII. Summary of systematic uncertainties in $Re(\epsilon'/\epsilon)$. See Tables I and II for more details on the errors from the $K \to \pi^+\pi^-$ and $K \to \pi^0\pi^0$ analyses, respectively.

Source	Error on $Re(\epsilon'/\epsilon)$ ($\times 10^{-4}$)	
	$K \to \pi^+\pi^-$	$K \to \pi^0\pi^0$
Trigger	0.23	0.20
CsI cluster reconstruction	$\cdots$	0.75
Track reconstruction	0.22	$\cdots$
Selection efficiency	0.23	0.34
Apertures	0.30	0.48
Acceptance	0.57	0.48
Backgrounds	0.20	1.07
MC statistics	0.20	0.25
Total	0.81	1.55
Fitting		0.31
Total		1.78

$$\frac{\Gamma(K^0 \to \pi^+\pi^-) - \Gamma(\bar{K}^0 \to \pi^+\pi^-)}{\Gamma(K^0 \to \pi^+\pi^-) + \Gamma(\bar{K}^0 \to \pi^+\pi^-)}$$
$$= (6.2 \pm 0.6) \times 10^{-6}. \tag{14}$$

We perform several checks of our result by dividing the data into subsets and checking the consistency of the $Re(\epsilon'/\epsilon)$ result in the various subsets. To check for time dependence, we break the data into 11 run ranges with roughly equal statistics. There are five run ranges in 1997 and six in 1999. Since the 1996 $K \to \pi^0\pi^0$ data do not have any corresponding $K \to \pi^+\pi^-$ data, we combine them with the neutral mode data in the first 1997 run range. As shown in Fig. 21, we find consistent results in all of the run ranges. The combined result for 1996 and 1997 data is $Re(\epsilon'/\epsilon) = [20.0 \pm 1.7(\text{stat})] \times 10^{-4}$, which can be compared directly to the KTeV03 result of $Re(\epsilon'/\epsilon) = [20.7 \pm 1.5(\text{stat})] \times 10^{-4}$ [20]. The decrease in statistical precision is due primarily to the removal of $K \to \pi^0\pi^0$ events with a cluster near one of the beam holes (see Sec. III C 3).

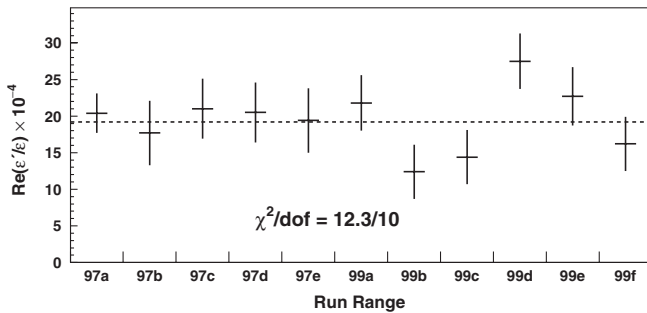
FIG. 21. $Re(\epsilon'/\epsilon)$ in subsets of the data sample. All points are statistically independent. The dashed line indicates the value of $Re(\epsilon'/\epsilon)$ for the full data sample. The 97a run range includes the 1996 $K \to \pi^0\pi^0$ data.

In 1999 we took data at high and low proton beam intensity so we are able to check for dependence of $Re(\epsilon'/\epsilon)$ on beam intensity. About 43% of the 1999 data were collected at low intensity (defined as less than 1.25×10^{11} protons/s) while 57% were collected at high intensity (greater than 1.25×10^{11} protons/s). The average proton rate in the low intensity sample is $\sim 1 \times 10^{11}$ protons/s and the average rate at high intensity is $\sim 1.6 \times 10^{11}$ protons/s. The average rate for 1996 and 1997 data is $\sim 1.5 \times 10^{11}$ protons/s. Figure 22 shows the 1999 $Re(\epsilon'/\epsilon)$ result for low and high intensities; there is no evidence for intensity dependence of the result.

Figure 22 also shows the value of $Re(\epsilon'/\epsilon)$ for the subsets of data with the regenerator in the left or right beam. We find no variation of $Re(\epsilon'/\epsilon)$ with regenerator position, which shows that there is no significant intensity difference between the two neutral beams and that there is no significant left-right asymmetry in the detector.

There are several cross-checks of the $K \to \pi^+\pi^-$ sample for which we do not divide the $K \to \pi^0\pi^0$ sample. We divide the $K \to \pi^+\pi^-$ sample based on the polarity of the analysis magnet and whether the tracks bend inward or outward in the magnet. In each of these cases, the $K \to \pi^0\pi^0$ sample is common to both data points and the errors are estimated by the difference in quadrature between the subset error and the nominal error. Figure 22 shows the $Re(\epsilon'/\epsilon)$ results for each of these subsets; they all show good agreement. The fit results for tracks that bend in or out in the magnet are both slightly larger than the nominal result; in this case other fit parameters have changed in each fit to allow the higher values of $Re(\epsilon'/\epsilon)$.

We check for dependence on kaon momentum by breaking the data into twelve 10 GeV/c momentum bins. In these fits, we fix the power-law dependence of the regeneration amplitude to the value found in the nominal fit. The
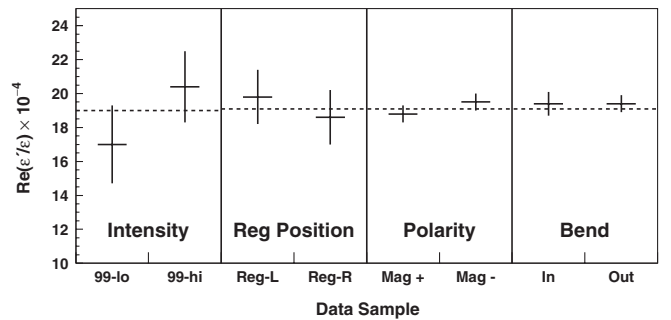

FIG. 22. $Re(\epsilon'/\epsilon)$ consistency with beam intensity, regenerator position, magnet polarity, and track bend. The intensity subsets are for the 1999 data only. Reg-left and reg-right refer to the position of the regenerator beam in the detector. These subsets are for the full data sample. Mag+ and Mag− are the magnet polarity and in/out are the bend of the two tracks in the magnet. In each of these subsets the $K \to \pi^0\pi^0$ sample is common to both fits; the errors are estimated by taking the quadrature difference with the error for the full data set. The dashed lines indicate the value of $Re(\epsilon'/\epsilon)$ in the appropriate full data sample.
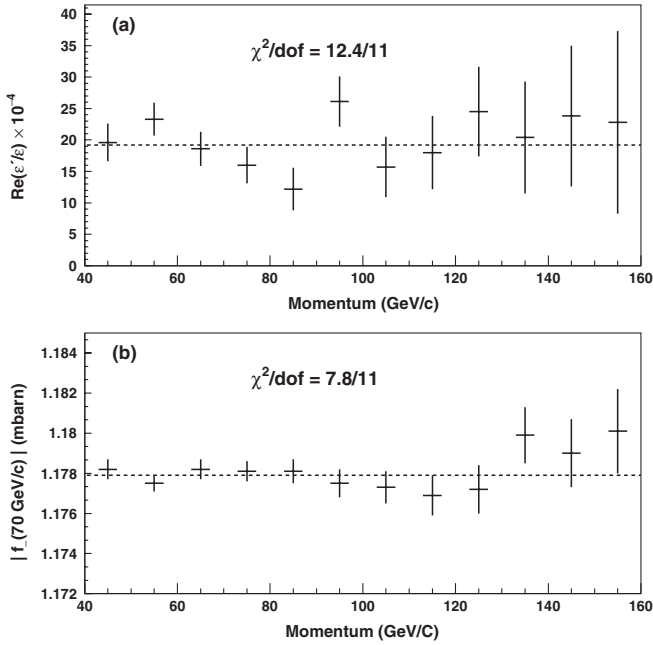
FIG. 23.   (a) $\mathrm{Re}(\epsilon'/\epsilon)$ and (b) $|f_-(70\ \mathrm{GeV}/c)|$ in 10 GeV/c momentum bins. All points are statistically independent. The dashed lines indicate the values for the full data sample.

free parameters are $\mathrm{Re}(\epsilon'/\epsilon)$, $|f_-(70\ \mathrm{GeV}/c)|$, and the charged and neutral kaon fluxes. Figure 23 shows the values of $\mathrm{Re}(\epsilon'/\epsilon)$ and $|f_-(70\ \mathrm{GeV}/c)|$ for these fits. We see no evidence for dependence of the $\mathrm{Re}(\epsilon'/\epsilon)$ result on kaon momentum.

Our value of $\mathrm{Re}(\epsilon'/\epsilon)$ is also consistent with other experimental results [16,17,19]. The weighted average of the new KTeV result with previous measurements is $\mathrm{Re}(\epsilon'/\epsilon) = [16.8 \pm 1.4] \times 10^{-4}$; see Fig. 24. The consistency probability of these results is 13%.
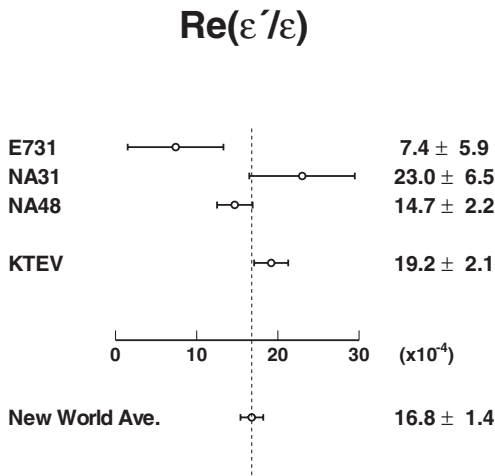

FIG. 24.   Final KTeV result for $\mathrm{Re}(\epsilon'/\epsilon)$ and comparisons with previous measurements from E731 [16], NA31 [17], and NA48 [19]. The new world average for $\mathrm{Re}(\epsilon'/\epsilon)$ is also shown.

B. Measurements of other kaon parameters

The regenerator beam decay distribution is sensitive to the kaon parameters τ_S, Δm, ϕ_ϵ, and $\mathrm{Im}(\epsilon'/\epsilon)$ [see Eq. (11)]. These parameters can be measured by fitting the decay vertex distribution in the regenerator beam. The analysis of the kaon parameters follows the general procedure developed in [16,18,20] but uses a new method to fit for all parameters simultaneously and apply the *CPT* constraints *a posteriori*.

The "z-binned" fit uses both charged and neutral mode data. The data are binned in 2 m wide z bins in the regenerator beam from 124 to 158 m. A single z bin from 110 to 158 m is used in the vacuum beam. As in the nominal $\mathrm{Re}(\epsilon'/\epsilon)$ fit, there are 24 free parameters for the charged and neutral kaon fluxes in each of 12 momentum bins and two free parameters for the regeneration amplitude and phase. Two additional parameters are used to fit the effective regenerator edge for the charged and neutral data to account for smearing effects near the edge.

The five kaon parameters τ_S, Δm, ϕ_ϵ, $\mathrm{Re}(\epsilon'/\epsilon)$, and $\mathrm{Im}(\epsilon'/\epsilon)$ are free parameters of the z-binned fit. The fit thus provides the most general description of the data with no requirement of *CPT* invariance. All systematic uncertainties are evaluated for the fit, accounting for correlations among the parameters. *CPT* invariance is imposed *a posteriori*, including the total errors of the parameters with their correlations, to obtain precise measurements of Δm and τ_S.

This approach allows a self-consistent analysis of the data with and without *CPT* constraints. The results are cross-checked following the procedure developed in [16,18,20], in which separate fits for Δm and τ_S were performed with *CPT* invariance imposed *a priori*.

1. Measurement of τ_S, Δm, ϕ_ϵ, and $\mathrm{Im}(\epsilon'/\epsilon)$ with no CPT constraint

The z-binned fit results are

$$\tau_S = [89.589 \pm 0.042_{\mathrm{stat}} \pm 0.056_{\mathrm{syst}}] \times 10^{-12}\ \mathrm{s}$$
$$= [89.589 \pm 0.070] \times 10^{-12}\ \mathrm{s},$$
$$\Delta m = [5279.7 \pm 12.8_{\mathrm{stat}} \pm 14.7_{\mathrm{syst}}] \times 10^6\ \hbar/\mathrm{s}$$
$$= [5279.7 \pm 19.5] \times 10^6\ \hbar/\mathrm{s},$$
$$\phi_\epsilon = [43.86 \pm 0.40_{\mathrm{stat}} \pm 0.49_{\mathrm{syst}}]^\circ = [43.86 \pm 0.63]^\circ,$$
$$\mathrm{Re}(\epsilon'/\epsilon) = [21.10 \pm 1.31_{\mathrm{stat}} \pm 3.17_{\mathrm{syst}}] \times 10^{-4}$$
$$= [21.10 \pm 3.43] \times 10^{-4},$$
$$\mathrm{Im}(\epsilon'/\epsilon) = [-17.20 \pm 9.04_{\mathrm{stat}} \pm 18.06_{\mathrm{syst}}] \times 10^{-4}$$
$$= [-17.20 \pm 20.20] \times 10^{-4}. \qquad (15)$$

The fit χ^2 is $\chi^2/\nu = 425.4/(432 - 33)$. The systematic uncertainties are summarized in Table VIII. The total uncertainty and the correlations among the parameters are

TABLE VIII. Systematic uncertainties for the global z-binned fit.

	$\tau_S \times 10^{-12}$ s	$\Delta m \times 10^6$ $\hbar$/s	ϕ_ϵ °	Re(ϵ'/ϵ) $\times 10^{-4}$	Im(ϵ'/ϵ) $\times 10^{-4}$
Charged trigger	0.004	2.4	0.08	0.13	1.16
Track reconstruction					
Maps	0.000	0.0	0.00	0.04	0.48
Resolution	0.001	2.6	0.08	0.10	1.20
p_t kick	0.009	0.7	0.00	0.14	1.75
Z DC	0.002	0.1	0.00	0.28	0.39
Selection efficiency					
p_t cut	0.008	3.6	0.10	0.16	0.96
Accidental	0.000	0.1	0.02	0.05	0.73
Scattering	0.001	0.3	0.10	0.15	0.17
Apertures					
Cell separation	0.036	10.0	0.31	0.42	2.57
Background	0.001	0.0	0.01	0.1	0.6
Acceptance					
Z slope	0.007	1.4	0.04	0.13	3.05
Neutral trigger	0.002	0.9	0.02	0.08	1.71
CsI reconstruction					
Energy linearity	0.003	0.8	0.01	2.30	2.43
Energy scale	0.008	0.8	0.01	1.72	12.29
Selection efficiency					
Ring	0.002	0.3	0.01	0.18	2.19
Pairing χ^2	0.012	2.2	0.07	0.02	2.19
Shape χ^2	0.0	0.2	0.02	0.06	0.90
Apertures					
CsI size	0.006	0.2	0.04	0.64	8.35
MA	0.	0.1	0.00	0.27	0.21
CA	0.	0.2	0.01	0.47	0.32
Background	0.008	0.3	0.04	0.43	6.69
Acceptance	0.002	0.1	0.01	0.13	2.81
Fitting					
Attenuation norm	0.003	0.3	0.01	0.01	0.01
Attenuation slope	0.003	2.1	0.05	0.05	0.00
Target K_S	0.026	4.7	0.11	0.00	0.00
Screening	0.018	5.6	0.02	0.57	1.35
Analyticity	0.0	0.0	0.25	0.0	0.0
MC statistics	0.016	4.9	0.15	0.36	2.78
Total syst	0.056	14.7	0.49	3.17	18.06
Stat error	0.042	12.8	0.40	1.31	9.04
Total error	0.070	19.5	0.63	3.43	20.20

evaluated following the procedure described in Appendix D of [20] and are given in Table IX. The correlations among these results are shown in Figs. 25 and 26.

Uncertainties from the charged mode are smaller than those from the neutral mode for the measurements of Δm, τ_S, and ϕ_ϵ. The measurement of these parameters is effectively a statistical average of the charged and neutral mode values, so it is dominated by the statistically larger charged mode. The measurements of Re(ϵ'/ϵ) and Im(ϵ'/ϵ) depend on the difference between the two modes, so the uncertainties from the statistically smaller neutral

data set are more important. Similarly, the fitting uncertainties have a much larger impact on Δm, τ_S, and ϕ_ϵ than on Re(ϵ'/ϵ) and Im(ϵ'/ϵ) since the uncertainties in the regeneration properties enter directly for the former and cancel for the latter.

There is a large correlation among τ_S, Δm, and ϕ_ϵ and also between Re(ϵ'/ϵ) and Im(ϵ'/ϵ). The correlation between Δm and ϕ_ϵ ($\rho = 82.8\%$) is somewhat reduced compared to the pure statistical correlation ($\rho = 97.3\%$), because the systematic uncertainty due to analyticity affects ϕ_ϵ but not Δm.

TABLE IX. Correlation coefficients for the z-binned fit.

	τ_S	Δm	ϕ_ϵ	$\mathrm{Re}(\epsilon'/\epsilon)$
Δm	-85.8%			
ϕ_ϵ	-76.5%	82.8%		
$\mathrm{Re}(\epsilon'/\epsilon)$	6.8%	-6.6%	2.5%	
$\mathrm{Im}(\epsilon'/\epsilon)$	-1.0%	2.6%	-4.1%	-46.5%

The measurement of $\mathrm{Im}(\epsilon'/\epsilon)$ can be expressed in terms of the phase difference:

$$\Delta\phi \approx -3\ \mathrm{Im}(\epsilon'/\epsilon) = [0.30 \pm 0.15_{\mathrm{stat}} \pm 0.31_{\mathrm{syst}}]^\circ$$
$$= [0.30 \pm 0.35]^\circ. \tag{16}$$

It is consistent with zero as expected from CPT invariance in a decay amplitude. The individual values of ϕ_{+-} and ϕ_{00} are

$$\phi_{+-} = [43.76 \pm 0.64]^\circ, \qquad \phi_{00} = [44.06 \pm 0.68]^\circ, \tag{17}$$

where the errors correspond to the total uncertainty and are calculated including the correlations reported in Table IX.

The superweak phase calculated using parameters from Eq. (15) is

$$\phi_{\mathrm{SW}} = [43.461 \pm 0.069_{\mathrm{stat}} \pm 0.070_{\mathrm{syst}}]^\circ$$
$$= [43.461 \pm 0.098]^\circ. \tag{18}$$

The difference between ϕ_ϵ and ϕ_{SW},

$$\delta\phi = \phi_\epsilon - \phi_{\mathrm{SW}} = [0.40 \pm 0.37_{\mathrm{stat}} \pm 0.42_{\mathrm{syst}}]^\circ$$
$$= [0.40 \pm 0.56]^\circ, \tag{19}$$

is also consistent with zero as expected from CPT invariance in $K^0 - \bar{K}^0$ mixing.

FIG. 26 (color online). $\Delta\chi^2 = 1$ contour for $\mathrm{Re}(\epsilon'/\epsilon)$ vs $\mathrm{Im}(\epsilon'/\epsilon)$ as measured by KTeV compared to the measurement of $\pi\pi$ phase shifts [2] and the CPT invariance expectation.

2. Measurement of τ_S and Δm with CPT constraint

Large correlations of Δm and τ_S with ϕ_ϵ increase the experimental uncertainties on these parameters. Assuming

$$\phi_\epsilon = \phi_{\mathrm{SW}}, \qquad \mathrm{Im}(\epsilon'/\epsilon) = 0, \tag{20}$$

as required by CPT invariance, significantly reduces the errors. This effect is illustrated in Fig. 25, which shows $\Delta\chi^2$ contours of total uncertainty for Δm, τ_S, and ϕ_ϵ with and without the CPT constraint.

The results are

$$\Delta m|_{\mathrm{cpt}} = [5269.9 \pm 12.3] \times 10^6\ \hbar/\mathrm{s},$$
$$\tau_S|_{\mathrm{cpt}} = [89.623 \pm 0.047] \times 10^{-12}\ \mathrm{s}, \tag{21}$$
$$\rho = -67.0\%,$$

where the errors correspond to the total experimental uncertainty and ρ is the correlation coefficient between Δm and τ_S. Compared to the determination without the CPT constraint, the uncertainty in Δm is reduced by a factor of ~ 1.5. Using these values of Δm and τ_S, we determine

$$\phi_{\mathrm{SW}}|_{\mathrm{cpt}} = [43.419 \pm 0.058]^\circ. \tag{22}$$

3. Kaon parameter cross-checks

We compare the new procedure to determine $\Delta m|_{\mathrm{cpt}}$ and $\tau_S|_{\mathrm{cpt}}$ to the one used in [20] in several steps. First the CPT constraint is applied using statistical uncertainties only; these results agree exactly with the fits in which the CPT constraints are included as in [20]. The value of Δm obtained using statistical uncertainties only, $\Delta m|_{\mathrm{stat\ cpt}} = 5266.5 \times 10^6 \hbar\ \mathrm{s}^{-1}$, is somewhat lower than for the determination using full uncertainties, Eq. (21). This difference can be traced to the above mentioned reduction in the correlation between Δm and ϕ_ϵ when systematic uncertainties are included.

Next, $\Delta m|_{\mathrm{cpt}}$ and $\tau_S|_{\mathrm{cpt}}$ are determined in the neutral and charged modes separately, as was done in KTeV03
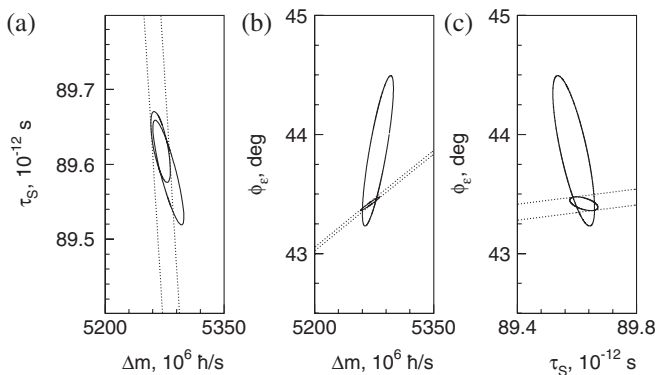

FIG. 25. $\Delta\chi^2 = 1$ contours of total uncertainty for (a) $\Delta m - \tau_S$, (b) $\phi_\epsilon - \Delta m$, and (c) $\tau_S - \phi_\epsilon$. Larger ellipses correspond to the z-binned fit without CPT invariance assumption. Dashed lines correspond to $\phi_\epsilon = \phi_{\mathrm{SW}}$ CPT constraint. Smaller ellipses are obtained after applying this constraint.
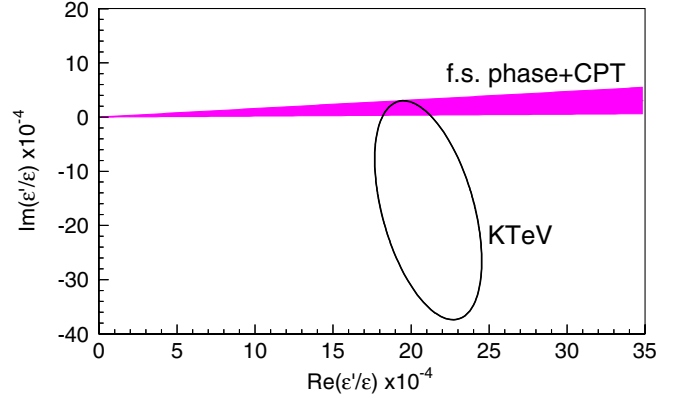
[20]. The resulting values are $\Delta m^{00} = (5257.6 \pm 8.3) \times 10^6 \; \hbar/s$, $\Delta m^{+-} = (5269.0 \pm 4.2) \times 10^6 \; \hbar/s$, $\tau_S^{00} = (89.667 \pm 0.039) \times 10^{-12}$ s, and $\tau_S^{+-} = (89.620 \pm 0.020) \times 10^{-12}$ s, where the superscript $+ - (00)$ stands for the charged (neutral) mode and the errors represent statistical uncertainties only. The measurements agree to within $1.3\sigma_{\text{stat}}$. Finally, the total uncertainties from Eq. (21) are compared to an evaluation in which the *CPT* constraints are embedded in the fit. They agree to within $\sim 10\%$, which is consistent with small changes in correlations among the fit parameters.

4. Determination of $K^0 - \bar{K}^0$ mass difference

KTeV measurements of the kaon system parameters can be used to determine the mass difference between K^0 and $\bar{K}^0$, which is zero in the absence of *CPT* violation. This test uses the Bell-Steinberger relation [30], which connects the *CP* and *CPT* violation in the mass matrix to the *CP* and *CPT* violation in the decay. Following the notation used in [31], the Bell-Steinberger relation can be written as

$$\left[\frac{\Gamma_S + \Gamma_L}{\Gamma_S - \Gamma_L} + i\tan\phi_{\text{SW}} \right] \left[\frac{\text{Re}(\epsilon)}{1 + |\epsilon|^2} - i\,\text{Im}(\delta) \right]$$
$$= \frac{1}{\Gamma_S - \Gamma_L} \sum_f A_L(f) A_S^*(f), \quad (23)$$

where the sum runs over all final states f and $A_{L,S}(f) \equiv A(K_{L,S} \to f)$. The parameter δ is related to the $K^0 - \bar{K}^0$ mass and decay width difference:

$$\delta = \frac{i(m_{K^0} - m_{\bar{K}^0}) + \frac{1}{2}(\Gamma_{K^0} - \Gamma_{\bar{K}^0})}{\Gamma_S - \Gamma_L} \cos\phi_{\text{SW}} e^{i\phi_{\text{SW}}}. \quad (24)$$

For neutral kaons, only a few decay modes contribute significantly to the sum in Eq. (23). The largest contribution comes from the $K_{L,S} \to \pi^+\pi^-$ and $K_{L,S} \to \pi^0\pi^0$ decay modes for which we can use KTeV measurements only; the other required measurements are the results from Eq. (15) and the $K_L \to \pi^+\pi^-$ and $K_L \to \pi^0\pi^0$ branching fraction measurements from KTeV [32]. The only external input needed is the value of τ_L. We use the Particle Data Group (PDG) average, which is based mainly on measurements from KLOE [33,34].

For the hadronic modes, we define

$$\alpha_i \equiv \frac{1}{\Gamma_S} A_L(i) A_S^*(i) = \eta_i B(K_S \to i),$$
$$i = \pi^0\pi^0, \; \pi^+\pi^-(\gamma), \; 3\pi^0, \; \pi^0\pi^+\pi^-(\gamma). \quad (25)$$

For the $K_L \to \pi^+\pi^-$ and $K_L \to \pi^0\pi^0$ decay modes we find

$$\alpha_{\pi^+\pi^-} = [(1124 \pm 13) + i(1077 \pm 13)] \times 10^{-6}, \quad (26)$$

$$\alpha_{\pi^0\pi^0} = [(481 \pm 7) + i(465 \pm 7)] \times 10^{-6}. \quad (27)$$

For the $K_L \to \pi^+\pi^-\pi^0$ and $K_L \to 3\pi^0$ decay modes we use the PDG values

$$\alpha_{\pi^+\pi^-\pi^0} = [(0 \pm 2) + i(0 \pm 2)] \times 10^{-6}, \quad (28)$$

$$|\alpha_{\pi^0\pi^0\pi^0}| < 7 \times 10^{-6} \quad \text{at 95\% C.L.} \quad (29)$$

For the semileptonic decay modes we use the definition and values from the PDG

$$\alpha_{\pi l \nu} \equiv \frac{1}{\Gamma_S} \sum_{\pi l \nu} A_L(\pi l \nu) A_S^*(\pi l \nu)$$
$$+ 2i \frac{\Gamma_L}{\Gamma_S} B(K_L \to \pi l \nu) \text{Im}(\delta) \quad (30)$$

and

$$\alpha_{\pi l \nu} = [(-2 \pm 5) + i(1 \pm 5)] \times 10^{-6}. \quad (31)$$

Combining the experimental data, we find from Eq. (23)

$$\text{Im}(\delta) = (-1.5 \pm 1.6) \times 10^{-5}. \quad (32)$$

The uncertainty in $\text{Im}(\delta)$ is 1.9×10^{-5} in the PDG average; the reduction of this error in Eq. (32) comes mainly from the more precise measurement of $\phi_\epsilon - \phi_{\text{SW}}$ from KTeV.

Combining the new determination of $\text{Im}(\delta)$ with the determination of $\text{Re}(\delta)$ and $\text{Im}(\delta)$ from the charge asymmetry in semileptonic decays [35],

$$\text{Re}(\delta) = (30 \pm 23) \times 10^{-5}, \quad \text{Im}(\delta) = (-660 \pm 650) \times 10^{-5},$$
$$\rho = -21\%, \quad (33)$$

we find

$$\text{Re}(\delta) = (25.1 \pm 22.5) \times 10^{-5},$$
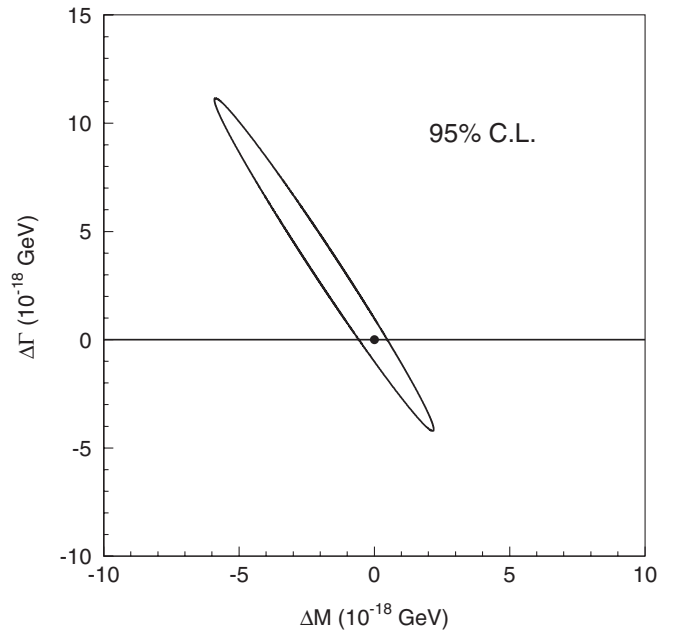$$\text{Im}(\delta) = (-1.5 \pm 1.6) \times 10^{-5} \quad (34)$$

FIG. 27.   Allowed region at 95% C.L. for ΔM and $\Delta\Gamma$.

with negligible correlation between the real and imaginary parts.

Using the value of δ from Eq. (34), we derive the allowed region for $\Delta M \equiv m_{K^0} - m_{\bar{K}^0}$ and $\Delta\Gamma \equiv \Gamma_{K^0} - \Gamma_{\bar{K}^0}$ as shown in Fig. 27. Assuming no *CPT* violation is present in the decay amplitudes, i.e. $\Delta\Gamma = 0$, we obtain the limit for the mass difference:

$$|M_{K^0} - M_{\bar{K}^0}| < 4.8 \times 10^{-19} \text{ GeV}/c^2 \quad \text{at 95\% C.L.} \quad (35)$$

VI. CONCLUSIONS

Using the full data sample of the KTeV experiment, we have made improved measurements of the direct *CP* violation parameter $\text{Re}(\epsilon'/\epsilon)$ and other parameters of the neutral kaon system. All of these results supersede previous KTeV results.

Assuming *CPT* invariance, we measure the direct *CP* violation parameter

$$\text{Re}\,(\epsilon'/\epsilon) = [19.2 \pm 1.1(\text{stat}) \pm 1.8(\text{syst})] \times 10^{-4}$$
$$= [19.2 \pm 2.1] \times 10^{-4}. \quad (36)$$

Also under the assumption of *CPT* invariance, we report new measurements of the $K_L - K_S$ mass difference and the K_S lifetime:

$$\Delta m = [5269.9 \pm 12.3] \times 10^6 \; \hbar/\text{s},$$
$$\tau_S = [89.623 \pm 0.047] \times 10^{-12} \text{ s.} \quad (37)$$

To test *CPT* symmetry, we measure the phase difference between the $K \to \pi^+\pi^-$ and $K \to \pi^0\pi^0$ decays to be

$$\Delta\phi = -3\,\text{Im}(\epsilon'/\epsilon) = [0.30 \pm 0.35]° \quad (38)$$

and the phase difference relative to the superweak phase to be

$$\phi_\epsilon - \phi_{\text{SW}} = [0.40 \pm 0.56]°. \quad (39)$$

These phase results are consistent with *CPT* invariance in both the decay amplitudes and $K^0 - \bar{K}^0$ mixing. Assuming no *CPT* violation in the decay amplitudes, we set a limit on the $K^0 - \bar{K}^0$ mass difference:

$$|M_{K^0} - M_{\bar{K}^0}| < 4.8 \times 10^{-19} \text{ GeV}/c^2 \quad \text{at 95\% C.L.} \quad (40)$$

After decades of experimental effort, direct *CP* violation in the neutral kaon system has now been measured with an uncertainty of about 10%. Considerable improvement in theoretical calculations of $\text{Re}(\epsilon'/\epsilon)$ will be required to take advantage of this experimental precision. There is some optimism [14], however, that future calculations using lattice gauge theory may approach a 10% uncertainty, making the precise measurement of ϵ'/ϵ an equally precise test of the standard model.

APPENDIX: SCREENING CORRECTIONS TO KAON REGENERATION AND ANALYTICITY

The measurements of ϕ_ϵ and Δm rely on an accurate determination of the regeneration phase. The regeneration phase is calculated from the momentum dependence of the regeneration amplitude using an analyticity relation. Regeneration in carbon, the principal material of the KTeV regenerator [36], is discussed here. We show how the momentum dependence of the regeneration amplitude, which is calculated based on the Regge theory with nuclear screening corrections, is checked using $K \to \pi\pi$ data. Based on this study, we derive the systematic uncertainties of the kaon parameters which are correlated with the determination of the regeneration phase.

In the Regge theory, for an isoscalar target and momenta above 10 GeV/c, the momentum dependence for the magnitude of the forward kaon-nucleon scattering amplitude difference for K^0 and $\bar{K}^0$ [Eq. (12)] is given by a single power law [28]:

$$|f_-^P(p)| = |f_-^P(70 \text{ GeV}/c)|\left(\frac{p}{70 \text{ GeV}/c}\right)^\alpha. \quad (A1)$$

Analyticity of the forward scattering amplitudes leads to a kaon momentum-independent phase of f_-^P given by

$$\arg(f_-^P) = -\pi\left(1 + \frac{\alpha}{2}\right). \quad (A2)$$

Therefore, α and $|f_-^P(70 \text{ GeV}/c)|$ determine $f_-^P(p)$ fully; they enter as free parameters in fits to KTeV data.

Kaon-nucleon interactions in carbon are screened due to rescattering processes. The effect of screening modifies the momentum dependence of $|f_-(p)|$ as well as its phase:

$$f_-(p) = f_-^P(p) \cdot \delta^{\text{sc}}(p)e^{i\phi^{\text{sc}}(p)}. \quad (A3)$$

Here $\delta^{\text{sc}}(p)$ and $\phi^{\text{sc}}(p)$ stand for screening corrections, which are evaluated using Glauber theory formalism [37,38] for diffractive scattering and using various models [39] for inelastic scattering. Elastic screening corrections are calculated with small theoretical uncertainties. Inelastic corrections, however, have a large spread of predictions as shown in Fig. 28. Since a momentum-independent change of $|f_-|$ does not modify $\arg(f_-)$, calculations of the screening corrections fix $\delta^{\text{sc}}(p) = 1$
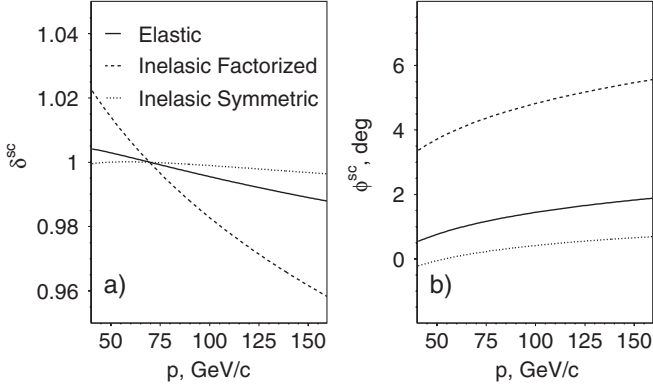
FIG. 28. Kaon momentum dependence of screening corrections to (a) the magnitude and (b) the phase of $f_-(p)$, for various models from [39]. The magnitude of each correction is defined to be 1 at 70 GeV/c.

for $p = 70$ GeV/c. Screening corrections calculated using the inelastic factorized model [39] are used for central values of all KTeV results in this paper.

As shown in Fig. 28, screening corrections modify the value of effective power law α from Eq. (A1). Since α is a free parameter of fits to the data, it is adjusted such that the net effect of the screening corrections is reduced. Figure 29(a) shows ratios of fitted [40] $|f_-(p)|$ using elastic and inelastic factorized screening models to fitted $|f_-^P(p)|$ using no screening corrections. Figure 29(b) shows the phase $\arg(f_-(p))$ obtained in these fits [41]. The screening correction thus results in up to a 0.5% adjustment of the regeneration amplitude and up to a 2° change in the regeneration phase, for the momentum range of the analysis. The values of α obtained in the fits with different screening models are given in Table X. Comparing χ^2/ν for these fits, one can see that the data rule out calculations without screening corrections and disfavor the inelastic symmetric screening calculation.
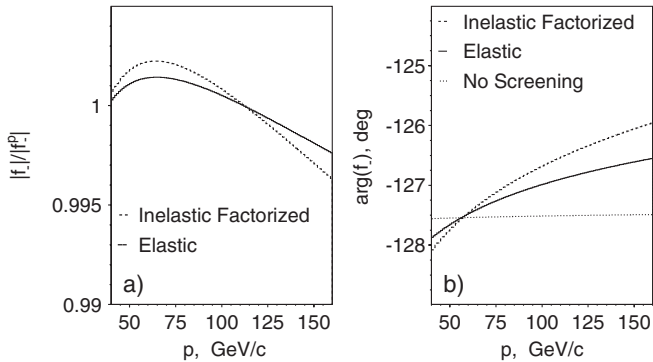

FIG. 29. Kaon momentum dependence of (a) the ratio of $|f_-(p)|$ from the fits using elastic (solid line) and inelastic factorized (dashed line) screening corrections to $|f_-^P(p)|$ from the fit using no screening corrections; (b) $\arg(f_-(p))$ from the fits with elastic (solid line), inelastic (dashed line) screening corrections, and with no screening corrections (dotted line).

TABLE X. Power-law coefficient α and χ^2/ν for fits using various screening models. The uncertainties given in parentheses are statistical errors.

	α	χ^2/ν
No screening	$-0.5813(5)$	471/399
Elastic screening	$-0.5715(5)$	431/399
Inelastic factorized screening	$-0.5376(5)$	425/399
Inelastic symmetric screening	$-0.5803(5)$	438/399

Comparison of Figs. 28 and 29 suggests significant sensitivity to the regeneration parameters and that the screening corrections may be determined directly from a fit to the $K \to \pi\pi$ data. In this fit, the magnitude of the regeneration amplitude, $|f_-(p)|$, is floated as a free parameter in each of the twelve 10 GeV/c momentum bins and is approximated to be constant within each bin. The regeneration phase $\arg(f_-(p))$ is calculated dynamically using the derivative analyticity relation (DAR) [42]:

$$\arg(f_-(p)) = -\pi - \tan\left(\frac{\pi}{2}\frac{d}{d\ln p}\right)\ln|f_-(p)|. \quad \text{(A4)}$$

In this calculation, $\arg(f_-(p))$ is estimated at an average of bin centers for the neighboring momentum bins, assuming that the bin-to-bin dependence of $|f_-(p)|$ is described by a power law. For momenta away from the bin centers, the phase is interpolated linearly. For example, the local power law at $p = 50$ GeV/c is calculated as

$$\alpha(50 \text{ GeV}/c) = -\frac{\ln\frac{|f_-(55 \text{ GeV}/c)|}{|f_-(45 \text{ GeV}/c)|}}{\ln\frac{55}{45}}. \quad \text{(A5)}$$

The phase $\arg(f_-(50 \text{ GeV}))$ is then given by Eq. (A2). This fit is referred to as the "DAR fit." Compared to the standard z-binned fit, the DAR fit has an additional $12 - 1$ free parameters.

Figure 30(a) compares ratios of $|f_-(p)|$ obtained from the DAR fit and from the fit using the inelastic factorized screening correction to $|f_-^P(p)|$ obtained from the fit using no screening corrections. There is a good agreement between the inelastic screening calculation and the DAR fit. The quality of the DAR fit ($\chi^2/\nu = 412/388$) is similar to that of the fit using inelastic screening corrections.

The data precision makes it possible to go one step further and float both $|f_-(p)|$ and $\arg(f_-(p))$ for each momentum bin; this fit is called the "phase fit." An overall phase cannot be measured this way, since it is 100% correlated with the value of ϕ_ϵ. Therefore the phase is fixed at $p = 75$ GeV/c to the value obtained in the DAR fit. The phase fit thus does not check an absolute prediction of the DAR fit but only the predicted momentum dependence. The quality of the phase fit is not improved compared to the DAR fit: For extra 11 degrees of freedom χ^2 is reduced by 7 units only. Figure 30(b) compares $\arg(f_-(p))$ calculated in the DAR fit and in the fit using the factorized inelastic screening correction as well as directly fitted in
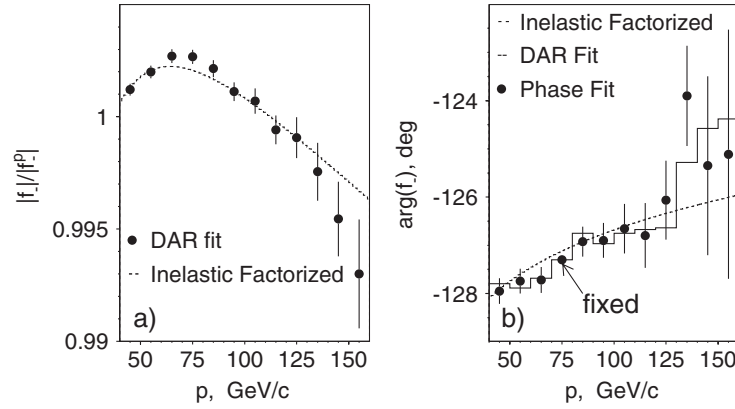
FIG. 30.   Kaon momentum dependence of (a) the ratio of $|f_-(p)|$ from the fit using inelastic factorized screening corrections (dashed line) and from the DAR fit (dots with error bars) to $|f_-^P(p)|$ from the fit using no screening correction; (b) $\arg(f_-(p))$ for the DAR fit (solid line), the phase fit (dots with error bars), and the fit using inelastic factorized screening model (dashed line). The phase fit is fixed to the DAR value for the 70 GeV/$c < p <$ 80 GeV/c momentum bin as indicated by the arrow.

the phase fit. These three different determinations are consistent with each other.

Note that the large correlation between $\arg(f_-)$ extracted at different momenta in the phase fit complicates a quantitative comparison between the predictions, so an additional test has been performed. The variation of $\arg(f_-)$ versus momentum, predicted by the DAR fit, shows an approximately linear dependence. The total variation, for the 40–160 GeV/c momentum range, is about 3°. As a cross-check, linear dependence of $\arg(f_-)$ is assumed:

$$\arg(f_-(p)) = \arg(f_-^P) + \alpha_R \frac{p - 70 \text{ GeV}/c}{120 \text{ GeV}/c}, \quad (A6)$$

where p is in GeV/c and α_R is an additional free fit parameter. A fit with $|f_-(p)|$ floated in 12 momentum bins using no screening corrections leads to significantly nonzero α_R: $\alpha_R = (3.1 \pm 0.6)°$. A similar fit, which includes the DAR phase correction, gives α_R consistent with zero: $\alpha_R = (0.2 \pm 0.6)°$.

In KTeV03 [20], the systematic uncertainties due to the screening corrections were evaluated by comparing the factorized and symmetric inelastic screening models which led to a large 0.75° error for ϕ_ϵ. In this analysis, the systematic uncertainties are determined directly from the data and estimated by comparing the fit based on the

inelastic factorized screening calculation with the DAR fit. For ϕ_ϵ, this evaluation leads to a small uncertainty of 0.02°; see Table VIII. The uncertainty is larger for Δm ($5.6 \times 10^{-12} \ \hbar/s$), since Δm is more sensitive to the variation of $\arg(f_-)$ as a function of the kaon momentum.

The determination of the regeneration phase relies on the validity of the analyticity assumption, Eq. (A2) [or equivalently of Eq. (A4)]. Various sources of deviation from Eq. (A2) were studied in [43]. The net effect of subleading Regge trajectories, uncertainties in f_- at low momentum, and electromagnetic regeneration in lead were estimated to be below 0.25°, which is taken as a systematic uncertainty for the regeneration phase. Note that an exchange of an odderon can affect the regeneration amplitude at high momentum but is not taken into account in this evaluation. The odderon contribution can be limited using pp and $p\bar{p}$ data; the best fit to these data gives a regeneration phase shift of $-(0.2 \pm 0.6)°$ [43].

A cross-check of the analyticity assumption is performed by measuring the asymmetry between $K \rightarrow \pi^- e^+ \bar{\nu}_e$ and $K \rightarrow \pi^+ e^- \nu_e$ decays downstream of the regenerator which is sensitive to the regeneration phase. Using approximately 125×10^6 decays, the difference between the measured $\arg(f_-)$ and the prediction based on analyticity is $[-0.70 \pm 0.88(\text{stat}) \pm 0.91(\text{syst})]°$ [44], which is consistent with the analyticity assumption.

[1] J. H. Christenson, J. W. Cronin, V. L. Fitch, and R. Turlay, Phys. Rev. Lett. **13**, 138 (1964).

[2] W. Ochs, PiN Newsletter **3**, 25 (1991).

[3] M. Kobayashi and T. Maskawa, Prog. Theor. Phys. **49**, 652 (1973).

[4] J. Ellis, M. K. Gaillard, and D. V. Nanopoulos, Nucl. Phys. **B109**, 213 (1976).

[5] F. J. Gilman and M. B. Wise, Phys. Lett. **83B**, 83 (1979).

[6] M. Ciuchini *et al.*, in *Kaon Physics*, edited by J. Rosner and B. Winstein (University of Chicago, Chicago, 2001), pp. 305–317.

[7] A. A. Belkov *et al.*, arXiv:hep-ph/9907335.

[8] J. Bijnens and J. Prades, J. High Energy Phys. 06 (2000) 035.

[9] T. Hambye *et al.*, Nucl. Phys. **B564**, 391 (2000).

[10] A. P. E. Pallante and I. Scimemi, Nucl. Phys. **B617**, 441 (2001).

[11] Y.-L. Wu, Phys. Rev. D **64**, 016001 (2001).

[12] S. Narison, Nucl. Phys. **B593**, 3 (2001).

[13] M. Sanchez, Ph.D. thesis, Universidad de Granada, 2003.

[14] A. J. Buras and M. Jamin, J. High Energy Phys. 01 (2004) 048.

[15] A. Pich, arXiv:hep-ph/0410215.

[16] L. K. Gibbons *et al.* (E731 Collaboration), Phys. Rev. Lett. **70**, 1203 (1993).

[17] G. D. Barr *et al.* (NA31 Collaboration), Phys. Lett. B **317**, 233 (1993).

[18] A. Alavi-Harati *et al.* (KTeV Collaboration), Phys. Rev. Lett. **83**, 22 (1999).

[19] A. Lai *et al.* (NA48 Collaboration), Eur. Phys. J. C **22**, 231 (2001).

[20] A. Alavi-Harati *et al.* (KTeV Collaboration), Phys. Rev. D **67**, 012005 (2003).

[21] J. Whitmore, Nucl. Instrum. Methods Phys. Res., Sect. A **409**, 687 (1998).

[22] A. J. Malensek, Fermilab Report No. FN-341 (errata), 1981.

[23] R. Brun *et al.*, GEANT 3.21, CERN, Geneva, 1994.

[24] S. Agostinelli *et al.*, Nucl. Instrum. Methods Phys. Res., Sect. A **506**, 250 (2003).

[25] E. Abouzaid *et al.* (KTeV Collaboration), Phys. Rev. D **78**, 032009 (2008).

[26] C. Bown *et al.*, Nucl. Instrum. Methods Phys. Res., Sect. A **369**, 248 (1996).

[27] L. K. Gibbons *et al.*, Phys. Rev. D **55**, 6625 (1997).

[28] F. Gilman, Phys. Rev. **171**, 1453 (1968).

[29] W.-M. Yao *et al.*, J. Phys. G **33**, 1 (2006).

[30] J. S. Bell and J. Steinberger, in *Proceedings of the Oxford International Conference on Elementary Particles*, edited by R. G. Moorhous *et al.* (Rutherford High Energy Lab, Chilton, Didcot, 1965), pp. 195–208 and 221–222.

[31] F. Ambrosino *et al.* (KLOE Collaboration), J. High Energy Phys. 12 (2006) 011.

[32] T. Alexopoulos *et al.* (KTeV Collaboration), Phys. Rev. D **70**, 092006 (2004).

[33] F. Ambrosino *et al.* (KLOE Collaboration), Phys. Lett. B **632**, 43 (2006).

[34] F. Ambrosino *et al.* (KLOE Collaboration), Phys. Lett. B **626**, 15 (2005).

[35] C. Amsler *et al.* (Particle Data Group), Phys. Lett. B **667**, 1 (2008).

[36] Total regeneration amplitude of the KTeV regenerator includes small corrections from regeneration in hydrogen and lead. For simplicity, these corrections are neglected in the following discussion.

[37] R. Glauber, Phys. Rev. **100**, 242 (1955).

[38] V. Franco and R. Glauber, Phys. Rev. **142**, 1195 (1966).

[39] L. Bertocchi and D. Treleani, Nuovo Cimento Soc. Ital. Fis. A **50**, 338 (1979).

[40] All fits discussed in this section are *z*-binned fits with no *CPT* constraint; see Sec V B.

[41] Note that the small variation of the phase for the fit using no screening corrections is caused by the regeneration in hydrogen.

[42] U. Sukhatme, G. L. Kane, R. Blankenbecler, and M. Davier, Phys. Rev. D **12**, 3431 (1975).

[43] R. A. Briere and B. Winstein, Phys. Rev. Lett. **75**, 402 (1995).

[44] G. C. Bown, Ph.D. thesis, University of Chicago, 2004.